HIGH PERFORMANCE INDUCTION MACHINE CONTROL: METHODS, LIMITS AND SOLUTIONS

BY

VEYSEL TUTKU BUYUKDEGIRMENCI

THESIS

Submitted in partial fulfillment of the requirements
for the degree of Master of Science in Electrical and Computer Engineering
in the Graduate College of the
University of Illinois at Urbana-Champaign, 2011

Urbana, Illinois

Adviser:

Professor Philip T. Krein

ABSTRACT

This thesis discusses various high performance induction machine control methods and provides methods for improved performance. Parameter sensitivity analyses on the discussed control methods are given. Practitioners have reported performance degradation during high speed DTC operation, including excessive torque ripple and diminished torque capability of the drive method. Asymptotic-input-output-decoupling is proposed to improve this erratic DTC performance. The results show that asymptotic decoupling compensates for erratic DTC performance with minimal control effort and controller complexity. This improvement trades off voltage headroom for torque regulation dynamics. Maximum instantaneous torque capabilities and related control strategies that can deliver high momentary forces are presented. The analyses show that by using the entire voltage headroom, in principle, up to 300% of the breakdown torque can be obtained at stall condition without saturating the magnetic circuit. An augmented vectorized volts-per-hertz control strategy is proposed and shown to provide high instantaneous torques comparable to that obtained with vector controllers.

To my parents, for their love and support, and to those who (un)intentionally contributed to this work

ACKNOWLEDGMENTS

I would like to express my utmost gratitude to my adviser, Professor Philip Krein, for giving me the life-changing opportunity to continue my education at the University of Illinois at Urbana-Champaign. It is an honor to conduct research under him. I appreciate and recognize his guidance and attention throughout my studies. I will always treasure his influence on being concise in communications. I hope to maintain it throughout my life.

I would like to thank the Grainger Center for Electric Machinery and Electromechanics for their generous support.

I have been incredibly fortunate to have Joyce Mast help me develop writing skills and keep my statements succinct. I express my great appreciation to Dr. Ali Bazzi and Pradeep Shenoy for their collaboration in conducting research. I would like to extend my special thanks to my office mate, Matt Magill, for helping me patiently to articulate my thoughts.

Finally, all my accomplishments would be impossible without the guidance of my loving parents. I am extremely grateful for their influence that led me to become the person I am today.

TABLE OF CONTENTS

LIST OF TABLES

LIST OF FIGURES

LIST OF ABBREVIATIONS

PWM	Pulse Width Modulation
FOC	Field Oriented Control
DFOC	Direct Field Oriented Control
IFOC	Indirect Field Oriented Control
DTC	Direct Torque Control
DSC	Direct Self Control
IOD	Input Output Decoupling
AIOD	Asymptotic Input Output Decoupling
MTA	Maximum Torque-per-Ampere Control

LIST OF SYMBOLS

J	Electric Current Density
B	Magnetic Field Density
F	Electromagnetic Force Density
d	Direct Axis Component
q	Quadrature Axis Component
0	Zero Axis Component
s	Stator
r	Rotor
m	Mutual
λ	Magnetic Flux Linkage
i	Current
v	Voltage
n_p	Number of Pole-Pairs
T_e	Electromagnetic Torque
T_L	Load Torque
r	Resistance
L	Inductance
ω	Rotating Frame Angular Velocity
J	Moment of Inertia
Ψ	Magnetic Flux Linkage Magnitude

ρ	Reference Frame Angle
σ	Machine Leakage Factor
ω_{slip}	Slip Frequency
τ	Scaled Electromagnetic Torque
ϕ	Flux Linkage Magnitude Squared
η	Reactive Torque
e_τ	Torque Error Manifold
e_ϕ	Flux Error Manifold
u_τ	Torque Command
u_ϕ	Flux Command

CHAPTER 1

INTRODUCTION

The objective of this thesis is to improve both the theoretical and practical understanding of high performance induction machine drive systems. Generic induction machine models are derived. An overview of common control methods for induction machines and parameter sensitivities is presented. Based on the machine models and controller derivations, performance evaluation and improvement methods are proposed and experimentally verified. In addition, maximum capabilities of the existing methods are investigated. Based on this investigation, an augmentation algorithm is proposed and shown to provide high momentary torque capabilities comparable to existing drives with less complexity.

Most common induction machine control methods are derived using the generic induction machine arbitrary reference frame model as presented by Krause [1]. Control methods for induction machines can be generalized into two categories—scalar and vector control. The scalar method focuses on steady-state performance. The machine's transient response is excluded. In addition, to avoid saturation, the applied voltage is limited below the *base speed*. This causes scalar controller torque capability to be limited by the rated current even if the voltage is below the rated value.

Vector controllers are known to provide much faster dynamic response and higher capabilities. Blaschke originated field-oriented control (FOC) [2], subsequently interpreted as a control based on dq transformation into a rotor flux frame. Another vector control method, direct torque control (DTC), was introduced by Takahashi and Noguchi [3] and Depenbrock [4]. These two methods are the most successful present control methods for high performance motion actuation. They were developed from a fundamental induction machine understanding and without a mathematical foundation [5]. Both FOC and DTC suffer from several implementation issues. Under parameter uncertainty, robust operation with FOC is out of the question.

Likewise, stator resistance information is imperative for DTC.

Discussions of DTC implementation and performance enhancement are presented based on this background information and derivations. Along with the implementation methods, performance limitations of DTC are investigated and experimentally verified. A robust, speed- and torque-dependent compensation approach is proposed and shown to enhance DTC at high speeds and high loads, at a cost of slower dynamic response.

Obtaining high momentary force is important in applications such as electromagnetic launch, rapid traction acceleration and other time-limited cases. This is accomplished using vector controllers, including FOC and DTC, but they limit voltage headroom and reduce instantaneous peak torque capabilities at high speeds. The maximum capabilities of these methods are investigated with the aid of symbolic software tools such as *Mathematica*. Nonlinear constraint optimization algorithms are employed to maximize the electromagnetic torque generated under rated stator voltages. An alternative high performance augmented scalar controller that uses the entire voltage headroom without saturating the machine is proposed and shown to provide high momentary torques comparable to those possible with direct torque control (DTC) and field-oriented control (FOC).

Detailed induction machine models in different reference frames and state-frames are presented for each control algorithm in Chapter 2. Chapter 3 elaborates on DTC theory based on [6] and [7] and gives generic performance improvement techniques and implementation approaches. Maximum torque capabilities of recent vector controllers are analyzed and compared in Chapter 4. Along with the investigation of controller limitations, an augmented volts-per-hertz (V/f) controller derivation and implementation is presented. Finally, Chapter 5 presents concluding remarks and highlights potential future work.

CHAPTER 2

BACKGROUND INFORMATION

Induction machines dominate industry applications because of their rugged structure, but they are relatively difficult to use in high performance applications requiring precise and robust speed, torque, and position control. For such applications, a drive designer needs sufficient knowledge about the machine. Hence, an accurate model is necessary. In Chapter 2, an induction machine model is introduced, and reduced order modeling using singular perturbation theory is discussed. Along with the model introduced, derivations of various control methods [8] are presented in this chapter.

Modeling is complicated, owing to nonlinearities in induction machines. For example, the flux linking certain rotor bars is dependent on rotor position. This introduces rotor-angle dependency into the mutual inductances, makes it difficult to model the system [1] and implement a real-time controller.

Park introduced reference frame theory and transformed the stator variables of a synchronous machine into a frame that is fixed in the rotor [9]. This approach revolutionized electric machine analysis by eliminating the position dependence [1]. Brereton applied Park's transformation to induction machines and developed a model in the rotor reference frame [10]. Krause et al. have shown that the rotor frame is not fundamental and the machine model can be obtained in arbitrary frames using one general transformation that eliminates the time-varying inductances. This is achieved by referring the stator and rotor variables to a reference frame at arbitrary angular velocity [1, 11].

In Section 2.1, a generalized two-phase dynamic equivalent model of an induction machine in the arbitrary reference frame is derived. Singular perturbation theory for model reduction is discussed in Section 2.2. Using the induction machine models derived, different controller types are introduced in Sections 2.3–2.4. The comparison and performance evaluation are the topics of Section 2.5.

2.1 Induction Machine Modeling

Elimination of position dependence is obtained through reference frame transformations. A well-known model for a symmetrical, 3-phase squirrel cage induction machine model in an arbitrary reference frame is given by Krause et al. [1, 11]. The flux linkage equations of the machine were expressed by Krause as

$$\begin{aligned}
\frac{d\lambda_{qs}}{dt} &= v_{qs} - r_s i_{qs} - \omega\lambda_{ds} \\
\frac{d\lambda_{ds}}{dt} &= v_{ds} - r_s i_{ds} + \omega\lambda_{qs} \\
\frac{d\lambda_{0s}}{dt} &= v_{0s} - r_s i_{0s} \\
\frac{d\lambda_{qr}}{dt} &= v_{qr} - r_r i_{qr} - (\omega - n_p\omega_r)\lambda_{dr} \\
\frac{d\lambda_{dr}}{dt} &= v_{dr} - r_r i_{dr} + (\omega - n_p\omega_r)\lambda_{qr} \\
\frac{d\lambda_{0r}}{dt} &= v_{0r} - r_r i_{0r}.
\end{aligned} \tag{2.1}$$

Variables ω, λ, r, i, and u are the mechanical speed, flux linkage, resistance, current, and voltage, respectively. Subscripts s and r denote stator and rotor, while d, q and 0 denote the direct, quadrature and zero components of the vector in the stationary reference frame.

The flux linkage in the stator and rotor were expressed by Krause as algebraic relationships:

$$\begin{aligned}
\lambda_{ds} &= L_{ls} i_{ds} + L_m(i_{ds} + i'_{dr}) \\
\lambda_{qs} &= L_{ls} i_{qs} + L_m(i_{qs} + i'_{qr}) \\
\lambda_{0s} &= L_{ls} i_{0s} \\
\lambda'_{dr} &= L'_{lr} i'_{dr} + L_m(i_{ds} + i'_{dr}) \\
\lambda'_{qr} &= L'_{lr} i'_{qr} + L_m(i_{qs} + i'_{qr}) \\
\lambda'_{0r} &= L'_{lr} i'_{0r},
\end{aligned} \tag{2.2}$$

where L stands for inductance and the subscripts l and m denote leakage and mutuality, respectively. A machine equivalent circuit in an arbitrary reference frame is given in Fig. 2.1 and can be obtained by combining (2.1) and algebraic flux linkage relationships (2.2). Allowing for variation in the

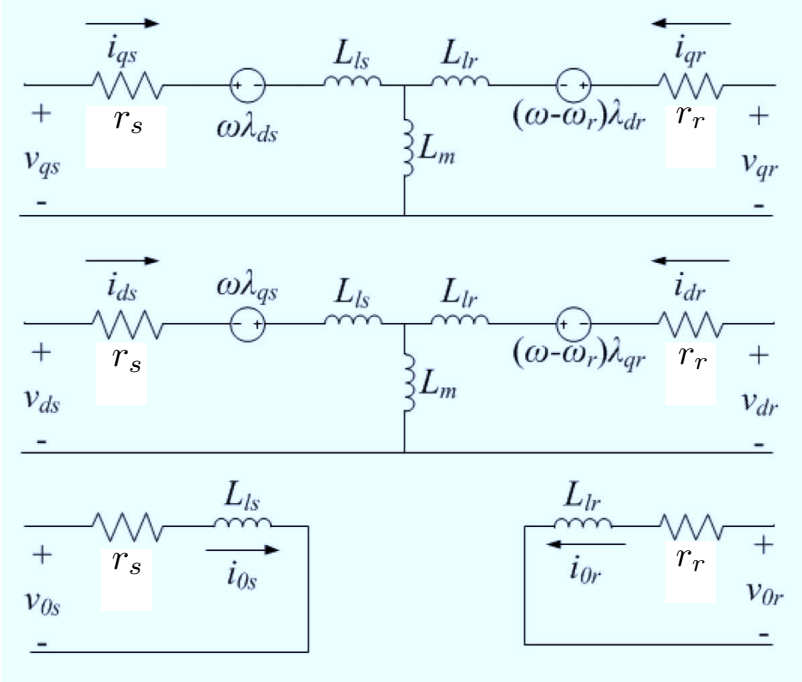

Figure 2.1: Induction machine model in an arbitrary reference frame as in [12].

transformation angle, this model may be expressed in rotor, synchronous or stationary reference frames by choosing ω to be rotor electrical frequency (ω_r), stator electrical frequency (ω_s) or zero, respectively.

Before proceeding with control methods, background information about singular perturbation theory and the use of this theory in induction machine modeling will be discussed in Section 2.2. Derivations of induction machine control methods will be presented in Section 2.3 using singular perturbation theory and reference frame theory.

2.2 Singular Perturbation Theory

Singularly perturbed systems were represented by Khalil as

$$\dot{x} = f(x, z, \sigma, u) \tag{2.3a}$$

$$\sigma\dot{z} = g(x, z, \sigma, u). \tag{2.3b}$$

where σ is a small parameter. Model reduction can be achieved for small perturbation parameters. For a perturbation parameter that is infinitely small, the differential equation in (2.3b) degenerates into the algebraic or transcendental equation $0 = g(x, z, 0, u)$. The advantage of this theory is that the discontinuity of solutions can be avoided if analyzed in multi-time scales. This approach allows the system order to be reduced and gives multiple models in different time scales for the reduced order system [13].

In such a system, the slow reduced model is associated with a time scale (t) and fast reduced model with ($t_f = t/\sigma$). The slow variables (x) behave like parameters in the fast time scale. In the slow time scale, the fast variables (z) follow the zero order manifold defined $0 = g(x, z, 0, u)$. The application of this theory to the stationary reference frame induction machine model will be presented in Section 2.3.

2.3 Induction Machine Control

The literature contains several different techniques [8, 14] for induction machine drives. These can be categorized into two groups according to their performance capabilities. Lower performance induction machine controllers are known as scalar controllers [15]. These are based on the steady-state model of the induction machine in the synchronous reference frame and significantly reduce the control effort. However, the focus of these methods is steady-state performance and transient response is unsatisfactory. Hence, scalar controllers are suitable only for applications requiring low performance.

Speed control in scalar methods is possible with several techniques. For a fixed frequency application, changing the voltage magnitude allows speed control, but the ranges are limited and the torque capability of the drive is reduced drastically. A wider operating range can be achieved by changing the stator excitation frequency, in other words, the synchronous speed. This method is the most common for low-performance variable-speed drive applications. Another method is slip control, but it requires a speed encoder [1, 15]. Better transient performance can be obtained with more sophisticated control structures based on the dynamic rather than the steady-state model.

Higher performance controllers are categorized as vector controllers [1, 7].

Their focus on dynamic models enables these methods to decouple input voltages and control the torque and flux separately. The generic idea behind these methods is to obtain direct or indirect flux and torque control. Field-oriented control (FOC) [2] was the first controller to achieve the desired control. Direct torque control (DTC) [3, 4] was presented 14 years after FOC and shown to compete with FOC from various control perspectives.

Several variations of these vector controllers have been presented [8]. These variations are known to improve system performance at the expense of parameter sensitivity. Vector controllers require machine knowledge in order to decouple the inputs and provide flux and torque/speed control. Therefore, parameter mismatches and sensitivity constitute a major concern in the drives area. In particular, rotor field-oriented controllers require rotor parameters which are extremely sensitive to temperature and difficult to measure. Several robust and adaptive control approaches have been presented to overcome this problem.

Several approaches can be implemented on a scalar or vector controller to optimize efficiency or maximize the torque for a given current. Efficiency optimization techniques or loss minimization techniques (LMT) optimize the machine flux to minimize the input current for a given load torque and speed [12]. Maximum torque-per-ampere (MTA) control is another method that can be implemented on a scalar or vector controller to optimize the torque while minimizing input current [16, 17, 18, 19]. Wasynczuk et al. introduced MTA to maximize steady-state torque for a given stator current [16]. In addition, Shin et al. introduced an approach to flux reference selection for maximum steady-state torque capability under field weakening [17].

Scalar controller derivation and performance characteristics will be discussed in Subsection 2.2.1. The most common vector control topologies, FOC and DTC, will be discussed in Subsections 2.2.2 and 2.2.3, respectively. Comparative performance evaluations along with parameter sensitivities provide sufficient insight about controller implementation in various cases and machine types. Practical issues encountered during implementation and utilization, such as erratic behaviors at high speed and high load [20] and very low speed operation, will be discussed. An extensive experimental performance evaluation of erratic behavior and solutions will be presented in Chapter 3.

2.3.1 Scalar Control

Using the arbitrary reference frame introduced by Krause, a machine model in the synchronous reference frame is obtained and given in (2.4).

$$\begin{aligned}
\frac{d\lambda_{qs}}{dt} &= v_{qs} - r_s i_{qs} - \omega_s \lambda_{ds} \\
\frac{d\lambda_{ds}}{dt} &= v_{ds} - r_s i_{ds} + \omega_s \lambda_{qs} \\
\frac{d\lambda_{qr}}{dt} &= -r_r i_{qr} - (\omega_s - n_p \omega_r)\lambda_{dr} \\
\frac{d\lambda_{dr}}{dt} &= -r_r i_{dr} + (\omega_s - n_p \omega_r)\lambda_{qr}.
\end{aligned} \tag{2.4}$$

The model shows that d axis stator flux is coupled with q axis flux and vice versa. An equivalent circuit representation of the induction machine model in the synchronous reference frame is given in Fig. 2.2. Since this model is in the synchronous reference frame, the steady-state solution for (2.4) is obtained by setting time derivatives equal to zero and was presented by Krein et al. [21] as

$$\lambda_{ds} = \frac{v_{qs}}{\omega_s} - \frac{r_s i_{qs}}{\omega_s} \tag{2.5a}$$

$$\lambda_{qs} = -\frac{v_{ds}}{\omega_s} + \frac{r_s i_{ds}}{\omega_s}, \tag{2.5b}$$

which shows that the magnitude of the stator flux linkage is proportional to the ratio of the stator voltage and the stator excitation frequency. This implies a control method as in (2.6). For a constant stator flux command, the torque-speed curve of a sample machine for different excitation frequencies can be obtained as given in Fig. 2.3. Ratings of the sample machine are 460 V, 3-ϕ, 10 HP and 40 A with a rated flux of 0.7 V·s.

$$|v_s| = \omega_s \lambda_s \tag{2.6a}$$

$$\frac{d\rho_s}{dt} = \omega_s \tag{2.6b}$$

Fig. 2.3 demonstrates that very small stator excitation frequencies result in degraded torque performance. Because the voltage magnitude is proportional to the stator frequency, the stator voltage magnitude becomes very small at low speeds. In such conditions the stator resistive voltage drop becomes

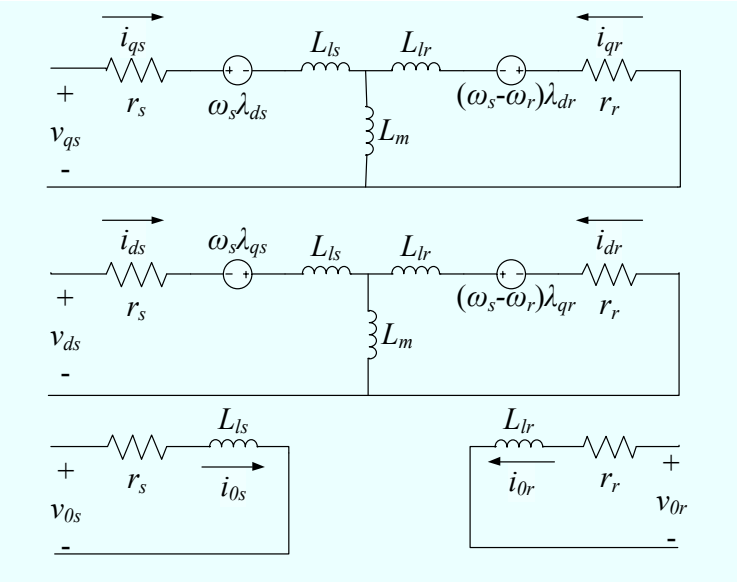

Figure 2.2: Induction machine model in the synchronous reference frame.

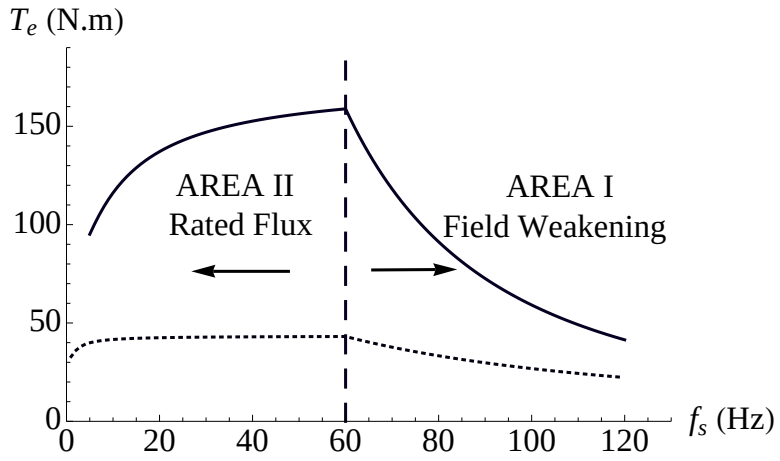

Figure 2.3: Breakdown (solid line) and rated (dashed line) torque-speed characteristic of a variable frequency scalar controller without resistive compensation.

significant and the peak torque that can be obtained from the induction machine is significantly reduced [8]. In order to avoid torque reduction at low speeds, a constant-magnetizing current control given in (2.7) can be used. The torque-speed curve for the constant magnetizing current control is given

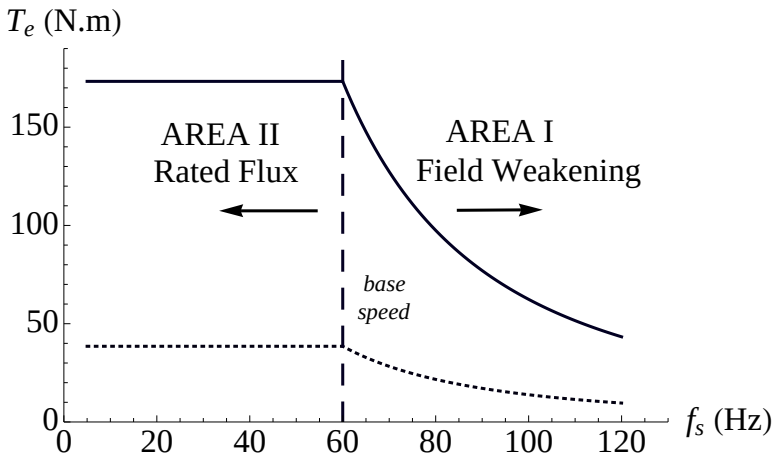

Figure 2.4: Breakdown (solid line) and rated (dashed line) torque-speed characteristic of a variable frequency scalar controller with resistive compensation.

in Fig. 2.4.

$$|v_s| = \omega_s \lambda_s + r_s |i_s| \tag{2.7a}$$

$$\frac{d\rho_s}{dt} = \omega_s \tag{2.7b}$$

In both controllers, Area I corresponds to operating speeds above base speed. Stator voltage is required to exceed the rated value to keep stator flux magnitude constant. If this is not possible, the stator voltage magnitude is kept constant while increasing the stator frequency. This phenomenon leads to reduced stator flux from (2.5). Hence, Area I is referred to as the *flux weakening region.*

The transient performance of a drive cannot be enhanced using a scalar controller because the only control variable, stator voltage magnitude, is insufficient to decouple the dq axes. However, the model in (2.5) enables a controller implementation that can supply decoupled input commands v_{ds} and v_{qs}. Instead of controlling the stator voltage magnitude, an accurate stator phasor angle which is obtained from rotor position guarantees decoupling. This approach forms the basis of vector control.

2.3.2 Field-Oriented Control

Coupling between the fluxes introduces degradation in the transient response. If some method could decouple the inputs to be applied to the machine, torque and flux regulation would become trivial. This idea resembles a dc machine structure which has separate inputs for flux and torque control. This idea was first introduced by Blaschke [2]. Existing decoupling approaches require stator or rotor flux angle estimation depending on the reference frame used. The control variables for such implementations are either the voltages to be applied or the currents to be enforced on the phases d and q.

Field oriented control was subsequently interpreted as a control based on dq transformation into a rotor flux frame. An induction machine model in the rotor reference frame is shown in Fig. 2.5. Drawing notation from Krein et al. [21] and using the state transformations

$$\begin{aligned}
\Psi &= \sqrt{\lambda_{dr}^2 + \lambda_{qr}^2} \\
i_q &= \frac{\lambda_{dr} i_{qs} - \lambda_{qr} i_{ds}}{\Psi} \\
i_d &= \frac{\lambda_{dr} i_{ds} + \lambda_{qr} i_{qs}}{\Psi} \\
\rho &= \arctan \frac{\lambda_{qr}}{\lambda_{dr}},
\end{aligned}$$

the machine equations are transformed into a frame in which the d axis is assigned to regulate rotor flux and the q axis to regulate electromagnetic torque. The machine model in terms of rotor flux linkages and stator currents in the rotor flux frame is

$$\begin{aligned}
\frac{d\omega}{dt} &= \frac{1}{J}(T_e - T_L) \\
\frac{d\lambda_{dr}}{dt} &= -\frac{r_r}{L_r}\lambda_{dr} - n_p\omega_r\lambda_{qr} + \frac{r_r}{L_r}L_m i_{ds} \\
\frac{d\lambda_{qr}}{dt} &= -\frac{r_r}{L_r}\lambda_{qr} + n_p\omega_r\lambda_{dr} + \frac{r_r}{L_r}L_m i_{qs} \\
\alpha\frac{di_{ds}}{dt} &= \frac{L_m r_r}{L_r^2}\lambda_{dr} + \frac{n_p\omega_r L_m}{L_r}\lambda_{qr} - \beta i_{ds} + v_{ds} \\
\alpha\frac{di_{qs}}{dt} &= \frac{L_m r_r}{L_r^2}\lambda_{qr} - \frac{n_p\omega_r L_m}{L_r}\lambda_{dr} - \beta i_{qs} + v_{qs},
\end{aligned} \tag{2.8}$$

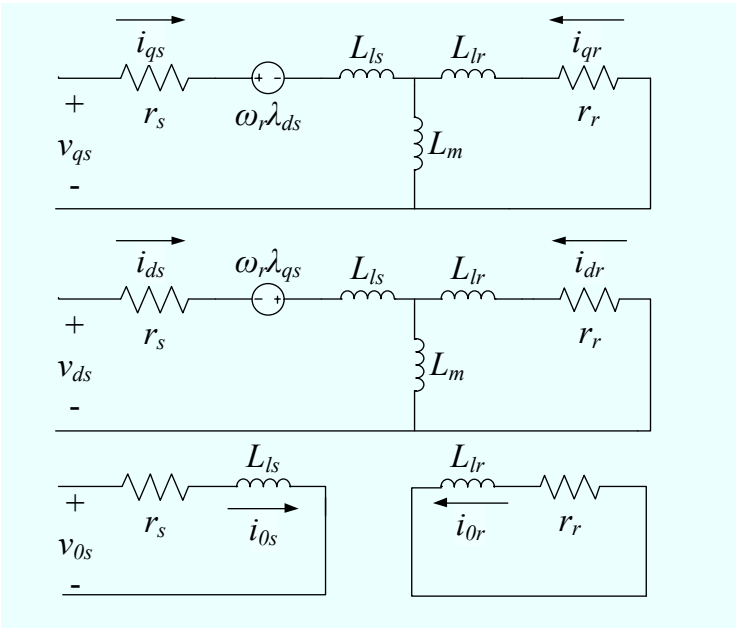

Figure 2.5: Induction machine model in the rotor reference frame.

where

$$\alpha = L_s - L_m^2/L_r$$
$$\beta = L_m^2 r_r/L_r^2 + r_s$$

Drawing notation from [21], dq stator voltages

$$v_{ds} = \alpha \left[-n_p\omega_r i_{qs} - \frac{L_m r_r}{L_r} i_{qs} \frac{(i_{qs}\lambda_{dr} - i_{ds}\lambda_{qr})}{\lambda_{qr}^2 + \lambda_{dr}^2} + \frac{\lambda_{dr} u_{flux} - \lambda_{qr} u_{speed}}{\sqrt{\lambda_{qr}^2 + \lambda_{dr}^2}} \right] - \frac{L_m}{L_r} n_p\omega_r\lambda_{qr} \tag{2.9a}$$

$$v_{qs} = \alpha \left[n_p\omega_r i_{ds} + \frac{L_m r_r}{L_r} i_{ds} \frac{(i_{qs}\lambda_{dr} - i_{ds}\lambda_{qr})}{\lambda_{qr}^2 + \lambda_{dr}^2} + \frac{\lambda_{dr} u_{speed} - \lambda_{qr} u_{flux}}{\sqrt{\lambda_{qr}^2 + \lambda_{dr}^2}} \right] + \frac{L_m}{L_r} n_p\omega_r\lambda_{dr} \tag{2.9b}$$

ensure decoupling in torque and flux regulation. In this equation u_{speed} and u_{flux} are defined as the decoupled speed and rotor flux command of the controller, respectively. As this is a direct method to regulate rotor flux, this

method is called direct-field-oriented control (DFOC).

DFOC requires a flux observer to keep track of the rotor angle in real time. This implies that stator and rotor time constants are required. Parameter mismatch in this process is a significant concern for DFOC. Even though rotor inductance is constant during the operation, it is very difficult to estimate its value. Moreover, the rotor resistance is subject to variations up to 100% [22]. Thus, an online rotor resistance estimation method or a model referenced adaptive controller (MRAC) is necessary to keep the system stable. That means robustness is compromised.

Several methods have been introduced to reduce rotor parameter sensitivity and improve torque response speed. A common one is to avoid rotor flux orientation and focus on stator fluxes. De Doncker et al. showed that FOC can be performed with air-gap [23] or stator flux [24, 25]. Stator field oriented control (SFOC) avoids rotor speed measurement, and can provide relatively fast torque response compared to DFOC. The importance of stator flux control for instantaneous torque generation is discussed in Chapter 3.

The field orientation methods discussed so far are voltage based methods. The implementation of these methods requires a fast switching frequency and online rotor or stator flux observation. All these problems can be avoided by using a current based approach. In the literature, such FOC implementations are known as indirect-field-oriented control (IFOC). This control method computes the i_d and i_q commands using the torque and flux references and the slip frequency from the reference values. The method requires a speed encoder. The stator position can be found as

$$\theta_s = \int_0^t (n_p \omega_r + \omega_{slip}) dt + \theta_0. \tag{2.10}$$

The i_d and i_q commands to be enforced can be computed by

$$\begin{aligned} i_{q,cmd} &= \frac{2L_r}{3n_p L_m} \frac{T_{cmd}}{\lambda_{cmd}} \\ i_{d,cmd} &= \frac{\lambda_{cmd}}{L_m} \\ \omega_{slip,cmd} &= \frac{r_r}{L_r} \frac{i_{qs}}{i_{ds}}, \end{aligned}$$

and employ a current source inverter (CSI) to enforce the computed currents.

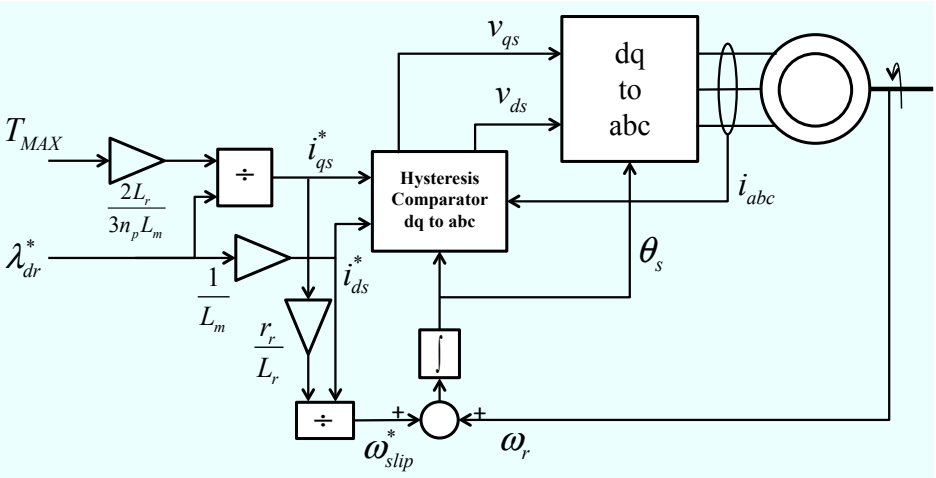

Figure 2.6: Indirect field oriented control implementation scheme.

A block diagram to represent this scheme can be seen in Fig. 2.6.

2.3.3 Direct Torque Control

A robust and less parameter-dependent vector control structure, direct torque control (DTC), was introduced in [3] and [4]. DTC, as typically implemented, regulates stator flux and electromagnetic torque in a hysteresis manner. Its implementation is presented using a switching table. Later authors [5, 6, 26] showed that the switching table is not fundamental to system implementation. A formal analytical framework is investigated and stability conditions are established [5, 27]. The discussion presented in this section derives largely from [6].

DTC is interpreted in [5, 6] as a sliding mode control of a singularly perturbed system, with the leakage factor (σ) as the perturbation parameter. Enforcing a sliding mode manifold on the torque and flux errors results in low sensitivity and reduced susceptibility to disturbances and plant parameter variations [28, 29]. In addition, this control structure combined with stator flux linkage control yields fast torque and flux regulation.

As explained in Section 2.2, induction machines can be considered as singularly perturbed systems. Equation (2.8) shows that for a low-leakage machine, stator currents are fast and fluxes are slow variables. An equivalent circuit representation of the singularly perturbed machine model in the

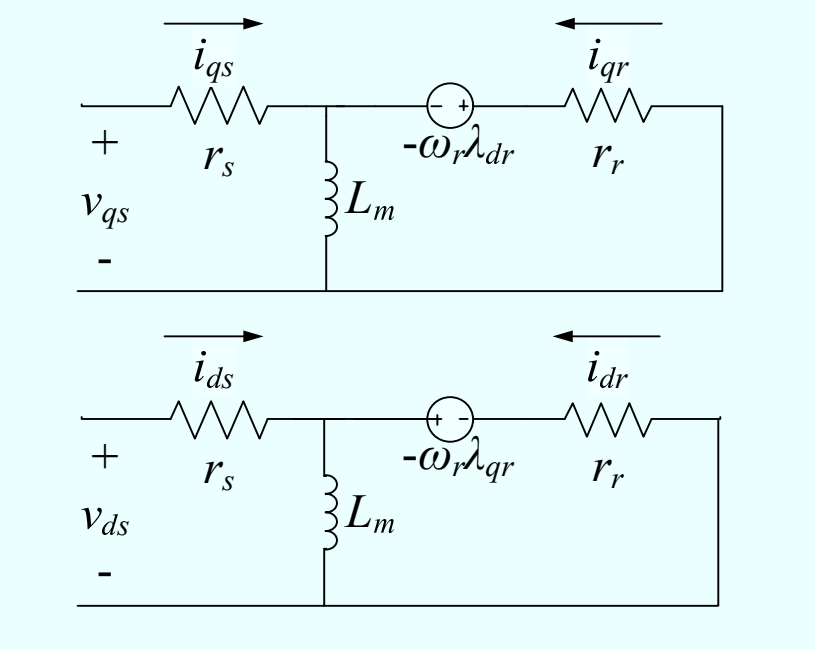

Figure 2.7: Induction machine model in the stationary reference frame with zero leakage.

stationary reference frame is obtained as in Fig. 2.7. For a torque control approach, the machine model is represented in the torque-flux framework presented by Sorchini [5] with the state transformations

$$\begin{aligned}
\tau &= \vec{\lambda}_s \times \vec{i}_s = \lambda_{ds} i_{qs} - \lambda_{qs} i_{ds} \\
\phi &= \lambda_{ds}^2 + \lambda_{qs}^2 \\
\rho &= \arctan(\lambda_{qs}/\lambda_{ds}) \\
\eta &= \vec{\lambda}_s \cdot \vec{i}_s = \lambda_{ds} i_{ds} + \lambda_{qs} i_{qs}.
\end{aligned}$$

The machine model in the torque-flux frame was obtained by Sorchini as

$$\begin{aligned}
\frac{d\omega}{dt} &= \frac{1}{J}(\frac{3}{2} n_p \tau - T_L) \\
\frac{d\phi}{dt} &= -2(r_s \eta - \sqrt{\phi} u_\phi) \\
\frac{d\rho}{dt} &= -r_s \frac{\tau}{\phi} + \frac{1}{\sqrt{\phi}} u_\tau
\end{aligned}$$

$$
\begin{aligned}
\sigma\frac{d\tau}{dt} &= -\frac{\gamma}{L_s}\tau - \frac{n_p}{L_s}\omega\phi + \frac{1}{L_s}\sqrt{\phi}u_\tau \\
&\quad + \sigma\left(n_p\omega\eta + \frac{1}{\sqrt{\phi}}(-\eta u_\tau + \tau u_\phi)\right) \\
\sigma\frac{d\eta}{dt} &= -\frac{\gamma}{L_s}\eta + \frac{r_r}{L_s L_r}\phi + \frac{1}{L_s}\sqrt{\phi}u_\phi \\
&\quad - \sigma\left(n_p\omega\tau + r_s\left(\frac{\eta^2+\tau^2}{\phi}\right) + \frac{1}{\sqrt{\phi}}(-\eta u_\phi - \tau u_\tau)\right).
\end{aligned}
$$

In this machine model, τ and η are only fast variables of the system. ϕ, ρ and ω are the slow variables where machine leakage (σ) is the perturbation parameter. The parameters σ and γ are

$$
\begin{aligned}
\sigma &= 1 - L_m^2/L_r L_s \\
\gamma &= r_r L_s/L_r + r_s.
\end{aligned}
$$

Sorchini defined a slow-reduced model for the induction machine

$$
\begin{aligned}
\frac{d\omega}{dt} &= \frac{1}{J}(\frac{3}{2}n_p\tau - T_L) \\
\frac{d\phi}{dt} &= -\frac{2r_s r_r}{\gamma L_r}\phi + 2\sqrt{\phi}\left(\frac{\gamma - r_s}{\gamma}\right)u_{\phi,slow} \\
\frac{d\rho}{dt} &= -r_s\frac{\tau}{\phi} + \frac{1}{\sqrt{\phi}}u_{\tau,slow} \\
0 &= -\frac{\gamma}{L_s}\tau - \frac{n_p}{L_s}\omega\phi + \frac{1}{L_s}\sqrt{\phi}u_{\tau,slow} \\
0 &= -\frac{\gamma}{L_s}\eta + \frac{r_r}{L_s L_r}\phi + \frac{1}{L_s}\sqrt{\phi}u_{\phi,slow},
\end{aligned}
\tag{2.11}
$$

and fast-reduced model

$$
\begin{aligned}
\frac{d\omega}{dt_f} &= 0 \\
\frac{d\phi}{dt_f} &= 0 \\
\frac{d\rho}{dt_f} &= 0 \\
\frac{d\tau}{dt_f} &= -\frac{\gamma}{L_s}\tau - \frac{n_p}{L_s}\omega\phi + \frac{1}{L_s}\sqrt{\phi}u_{\tau,fast} \\
\frac{d\eta}{dt_f} &= -\frac{\gamma}{L_s}\eta + \frac{r_r}{L_s L_r}\phi + \frac{1}{L_s}\sqrt{\phi}u_{\phi,fast}.
\end{aligned}
\tag{2.12}
$$

An appropriate control strategy can be derived to obtain instantaneous torque. However, system performance may degrade with a sufficiently large perturbation parameter. Therefore, a trade-off exists with the response speed and performance range.

The control inputs to achieve sliding mode control for such a system are

$$u_\tau = -k_\tau sgn(e_\tau) \tag{2.13a}$$

$$u_\phi = -k_\phi sgn(e_\phi). \tag{2.13b}$$

Given the input commands, the system follows the torque and flux error manifolds e_τ and e_ϕ, respectively. This approach can be transformed from the torque-flux frame back into the dq frame using the flux angle in (2.14).

$$\begin{bmatrix} u_\phi \\ u_\tau \end{bmatrix} = \begin{bmatrix} \cos(\rho) & \sin(\rho) \\ -\sin(\rho) & \cos(\rho) \end{bmatrix} \begin{bmatrix} u_{ds} \\ u_{qs} \end{bmatrix} \tag{2.14}$$

An equivalent representation is given in Fig. 2.8. The stator flux, angle and electromagnetic torque are estimated as follows:

$$\phi_s = \left| \int_0^t v_s - i_s r_s dt \right| \tag{2.15}$$

$$\rho_s = \arctan(\lambda_{qs}/\lambda_{ds}) \tag{2.16}$$

$$T_e = \frac{3}{2} n_p \vec{\lambda_s} \times \vec{i_s}. \tag{2.17}$$

2.4 Parameter Sensitivities

All vector controllers are subject to parameter sensitivities. Parameter sensitivity of a drive is caused by the reference frame, implementation and operating principles of the drive systems. For example, a controller operating in the rotor reference frame implies that the rotor time constant is important for implementation. Likewise, a controller in the stator frame leads to stator time constant or at least stator resistance dependency. The sensitivities of FOC and DTC are investigated in this section.

In a DFOC drive, the controller requires the rotor position to be observed in order to perform dq transformation and control. Equation (2.9) shows

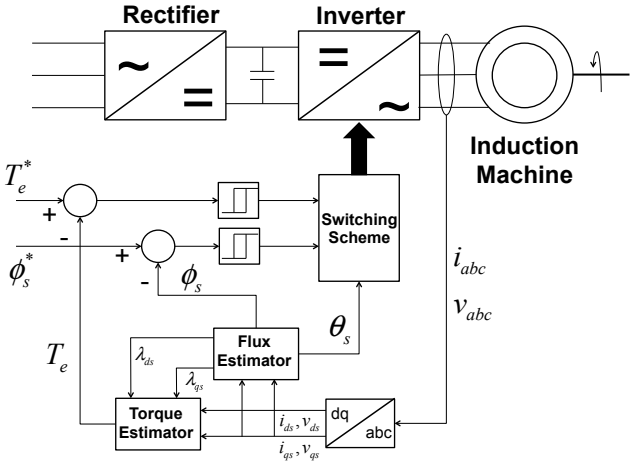

Figure 2.8: Direct torque control implementation scheme.

that the input voltages depend on almost all the machine parameters. The parameter sensitivity of the input voltages can be found by computing the sensitivity matrix. The input voltages v_d and v_q are re-written in (2.18) by generalizing the machine parameters.

$$v_{ds} = p_1[-n_p\omega_r i_{qs} - p_2p_3 i_{qs}\frac{i_q}{\Psi} + \frac{\lambda_{dr}u_{flux} - \lambda_{qr}u_{speed}}{\Psi}] - p_2 n_p\omega_r\lambda_{qr} \quad (2.18a)$$

$$v_{qs} = p_1[n_p\omega_r i_{ds} + p_2p_3 i_{ds}\frac{i_q}{\Psi} + \frac{\lambda_{dr}u_{speed} + \lambda_{qr}u_{flux}}{\Psi}] + p_2 n_p\omega_r\lambda_{dr}. \quad (2.18b)$$

Computing the jacobian of (2.18) leads to

$$\frac{\partial v}{\partial p} = \begin{bmatrix} -i_{qs}n_p\omega_r - p_2p_3\frac{i_{qs}i_q}{\Psi} + u_{flux}\frac{\lambda_{dr}}{\Psi} - u_{speed}\frac{\lambda_{qr}}{\Psi} & -n_p\omega_r\lambda_{qr} - p_1p_3\frac{i_{qs}i_q}{\Psi} & p_1p_2\frac{i_{qs}i_q}{\Psi} \\ i_{ds}n_p\omega_r + p_2p_3\frac{i_{ds}i_q}{\Psi} + u_{flux}\frac{\lambda_{qr}}{\Psi} - u_{speed}\frac{\lambda_{dr}}{\Psi} & n_p\omega_r\lambda_{dr} + p_1p_3\frac{i_{ds}i_q}{\Psi} & p_1p_2\frac{i_{ds}i_q}{\Psi} \end{bmatrix}$$

The Euclidian norm of this jacobian is given in (2.19).

$$\begin{aligned} \left\|\frac{\partial v}{\partial p}\right\| = \Bigg(&|i_s|^2\left(p_1^2(p_2^2+p_3^2)\frac{i_q^2}{\Psi^2} + (p_2p_3\frac{i_q}{\Psi} + n_p\omega_r)^2\right) \\ &+ \frac{2p_2p_3i_q}{\Psi^2}(u_{speed}i_d - u_{flux}i_q) + u_{flux}^2 + u_{speed}^2 \\ &+ n_p^2\omega_r^2\Psi^2 + 2n_p\omega_r(p_1p_3\frac{i_di_q}{\Psi^2} + u_{speed}\frac{i_d}{\Psi^2} - u_{flux}\frac{i_q}{\Psi^2}\Bigg)^{1/2} \end{aligned} \quad (2.19)$$

where the vector p is defined as

$$p = \begin{bmatrix} \sigma & \frac{L_m}{L_r} & r_r \end{bmatrix}.$$

The parameter sensitivity analysis for DTC drives is carried out for the torque and flux input commands defined in (2.13). The inputs and steady-state values of torque and flux can be defined as

$$\begin{aligned} u_\tau &= -k_\tau sgn(\tau - \tau_{ref}) \\ u_\phi &= -k_\phi sgn(\phi - \phi_{ref}) \\ \tau &= -p_1 n_p \omega \phi + p_1 \sqrt{\phi} u_\tau \\ \phi &= (p_2 u_\phi)^2 . \end{aligned}$$

The jacobian of the inputs can be computed as

$$\frac{\partial u}{\partial p} = \begin{bmatrix} -\frac{\tau \delta(e_\tau) k_\tau}{p_1(1+p_1\sqrt{\phi}\delta(e_\tau)k_\tau)} & 0 \\ 0 & -\frac{2\delta(e_\phi)k_\phi u_\phi^2}{1+2\delta(e_\phi)k_\phi p_2 u_\phi} \end{bmatrix} \tag{2.20}$$

where δ is defined as the dirac delta function. Vector p is defined as

$$p = \begin{bmatrix} \frac{1}{\gamma} & \frac{L_s}{r_s} \end{bmatrix}.$$

It can be seen that, as long as an error exists in the controller, the sensitivities of the input signals to γ and stator time constant (L_s/r_s) in torque-flux frame are negligible. On the sliding mode manifolds e_ϕ and e_τ, the input signals are highly parameter sensitive. However, the probability that the torque and flux regulation errors are zero is zero since these manifolds are defined as C^1 (continuously differentiable) functions within an open connected real set. A rigorous stator resistance sensitivity analysis is provided in Chapter 3.

CHAPTER 3

DIRECT TORQUE CONTROL: IMPLEMENTATION, PERFORMANCE AND SOLUTIONS

Since first introduced in [3, 4], direct torque control has become one of the most common vector control structures for induction machines. Given a sufficient supply voltage, DTC achieves fast torque and flux responses and provides robustness in contrast with FOC. The principle behind DTC was hysteresis control for both torque and flux of the machine [3], which restricts the torque and flux regulation errors of the drive system within a small band. However, the transient response and maximum capabilities are limited by the dc bus voltage. Therefore, several techniques for implementation are presented in the literature. These techniques are discussed in this chapter.

The idea of DTC can be elaborated by analyzing the electromagnetic torque in a symmetrical three-phase induction machine. The instantaneous torque can be expressed as the cross product of the stator flux linkage and stator current space vectors:

$$T_e = \frac{3}{2} n_p \vec{\lambda_s} \times \vec{i_s}. \tag{3.1}$$

With a DTC employing a voltage source inverter (VSI), it is possible to directly control stator, rotor or air-gap flux linkage along with torque. However, almost-instantaneous responses can be achieved by only stator flux linkage control. The reason is presented as follows.

Assuming that the magnitudes of stator and rotor flux linkages and stator currents are constant for a short time interval, stator flux linkage and current was restated in space vector form by Vas [7] as

$$\vec{\lambda_s} = |\vec{\lambda}_s| e^{j\rho_s}$$
$$\vec{i_s} = |\vec{i}_s| e^{j\alpha_s}$$

where ρ_s is the angle of the stator flux linkage space vector and α_s is the

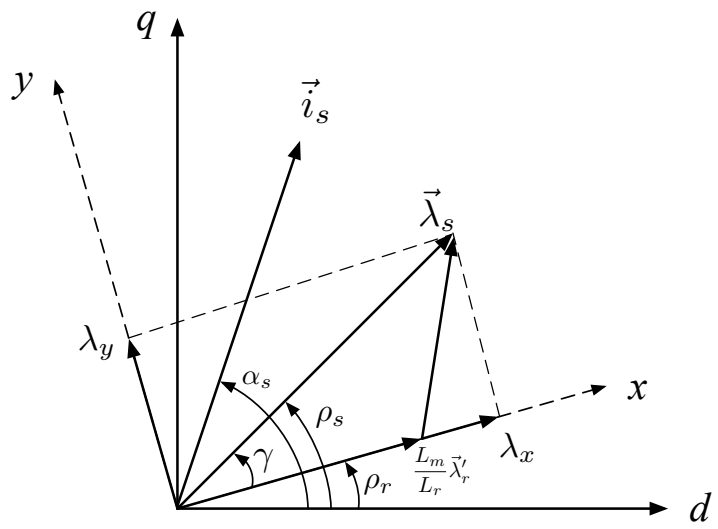

Figure 3.1: Demonstration of phasors in the rotor frame as in [7].

angle of the stator current space vector. Using the algebraic equations

$$\vec{\lambda_s} = L_s\vec{i_s} + L_m\vec{i'_r}$$
$$\vec{\lambda'_r} = L_r\vec{i'_r} + L_m\vec{i_s}$$

the torque expression can be transformed into

$$T_e = \frac{3}{2}n_p\frac{L_m}{L_sL'_r}\vec{\lambda_s} \times \vec{\lambda'_r} \tag{3.2}$$

In a vector control notation, all the phasors are transformed into the rotor reference frame as shown in Fig. 3.1. The stator flux can be separated into two components λ_x and λ_y, where λ_x is collinear with the rotor flux and λ_y is the component that produces torque. One important detail in this context is that in an FOC drive, the rotor currents are controlled to manipulate rotor flux, whereas in a DTC drive the flux linkages are the control quantities.

From Fig. 3.1 it can be seen that the electromagnetic torque depends on

the angle between the stator flux and rotor flux linkage space vectors:

$$\begin{aligned} T_e &= \frac{3}{2} n_p \frac{L_m}{L_s L'_r} |\lambda_s| |\lambda'_r| \sin(\rho_s - \rho_r) \\ &= \frac{3}{2} n_p \frac{L_m}{L_s L'_r} |\lambda_s| |\lambda'_r| \sin(\gamma). \end{aligned} \tag{3.3}$$

The rotor time constant of an induction machine is large; therefore, the change in the rotor flux linkage space vector angle is slow compared to the stator flux linkage space vector. Under such conditions, the time rate change of the electromagnetic torque is found by Vas as

$$\frac{dT_e}{dt} \approx \frac{3}{2} n_p \frac{L_m}{L_s L'_r} |\lambda_s| |\lambda'_r| \cos(\rho_s - \rho_r) \frac{d\rho_s}{dt}. \tag{3.4}$$

This shows that the electromagnetic torque time rate of change is proportional to the stator flux angle time rate of change. For a short transient assuming that the rotor flux is not changed, desired electromagnetic torque can be generated by rotating the stator flux space vector in a counter-clockwise direction (phase advancing) or clockwise direction (phase retarding) or by stopping its rotation [7]. In addition, since the rotor flux is generated by the stator traveling wave, such implementation for rotor flux control would be subject to a delay related to the rotor and stator time constants combined. Hence, stator flux linkage control achieves fast torque response.

3.1 Direct Torque Control Implementation

Direct control of stator flux angle achieves torque control. Several implementations exist that attempt to achieve this control. The transformations defined in (2.14) are used to map the torque-flux frame back into the dq frame in a continuous implementation [6]. However, the most common implementations are discrete methods. The generic idea behind these methods is to quantize the stator flux angle. Such implementations limit the possible number of space vectors to be enforced to the stator.

It is very important to emphasize a conflict about DTC implementation. All variable speed ac drives require an inverter stage. Generally these are hex bridges with eight different switch configurations that can be chosen. Six of

these configurations refer to non-zero output voltages. This fact is confused with six-step stator flux angle quantization in the literature. Thus six-step implementation is the most common method since its invention [3]. There exist six different non-zero voltage vectors in an inverter, but this is not a reason to be limited with six-sector space vector modulation. The number of sectors — the quantization resolution — for flux angle can be improved regardless of the inverter stage used, and any voltage waveform and level can be obtained subject to dc bus voltage available.

Six-step DTC can be implemented using a look-up table, which not only reduces the computation complexity but also achieves ease of implementation, at the expense of high torque and flux ripple. This look-up table in [3], the so-called optimum switching table, is used to decide whether the system needs to advance the phase angle to increase the output torque and whether the stator flux is to be augmented or weakened in order to reach the reference values. The derivation of this look-up table and the operating principle will be explained.

This six-step approximation is analogous to the transformation (2.14) with a 60^o stator flux angle quantization, although this is not required and DTC can be implemented using any kind of switching structure based on

$$\begin{aligned}
\frac{d\phi}{dt} &= -\frac{2r_s r_r}{\gamma L_r}\phi + 2\sqrt{\phi}\left(\frac{\gamma - r_s}{\gamma}\right) u_{\phi,slow} \\
\frac{d\tau}{dt_f} &= -\frac{\gamma}{L_s}\tau - \frac{n_p}{L_s}\omega\phi + \frac{1}{L_s}\sqrt{\phi}u_{\tau,fast} \\
\frac{d\eta}{dt_f} &= -\frac{\gamma}{L_s}\eta + \frac{r_r}{L_s L_r}\phi + \frac{1}{L_s}\sqrt{\phi}u_{\phi,fast}.
\end{aligned}$$

Assuming zero stator resistance, the stator flux linkage can be expressed as

$$\vec{V_s} = \frac{d}{dt}\vec{\lambda_s} = j|\vec{\lambda_s}|\frac{d\rho_s}{dt}. \tag{3.5}$$

Therefore, by selection of appropriate stator voltage space vector, the electromagnetic torque or the flux linkage magnitude can be changed rapidly, subject to available voltage. As given in Fig. 3.2, for a flux vector in Sector 1, the space vectors $\vec{u}_2$ and $\vec{u}_3$ will increase the torque, whereas $\vec{u}_5$ and $\vec{u}_6$ will decrease it. Likewise, the space vectors $\vec{u}_2$ and $\vec{u}_6$ will increase the flux linkage magnitude, whereas $\vec{u}_3$ and $\vec{u}_5$ will decrease it. This very idea is the

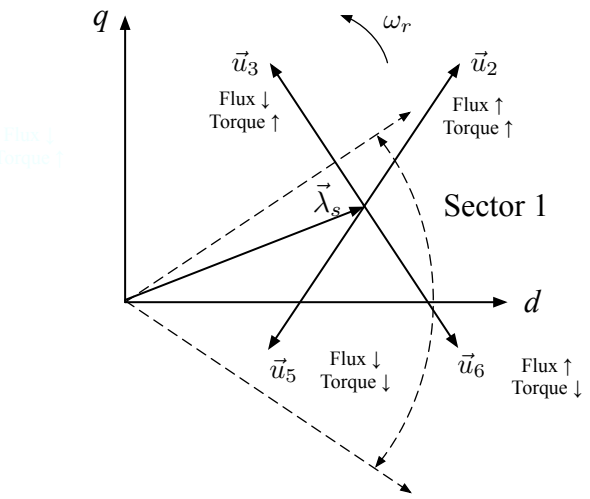

(a)

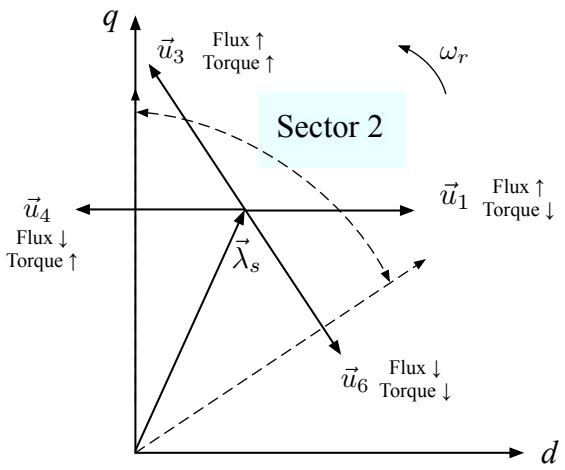

(b)

Figure 3.2: Switching vector selection in (a) Sector 1 and (b) Sector 2.

foundation behind the switching table employed in conventional DTC.

The inverter switching states are determined depending on the torque and flux errors of the drive. The limit cycle implementation with a hysteresis control enforces torque and flux ripple to be within error bands of $2\Delta T_e$ and $2\Delta\lambda$, respectively. The illustration of a flux phasor trajectory within the hysteresis band is demonstrated in Fig. 3.3(a). The inverter switching states are determined by Table 3.1, and the six-sector switching table is presented in Table 3.2 (as in [3]).

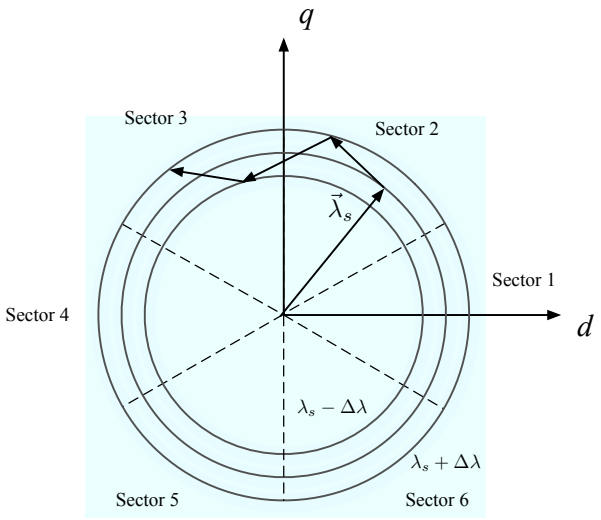

(a)

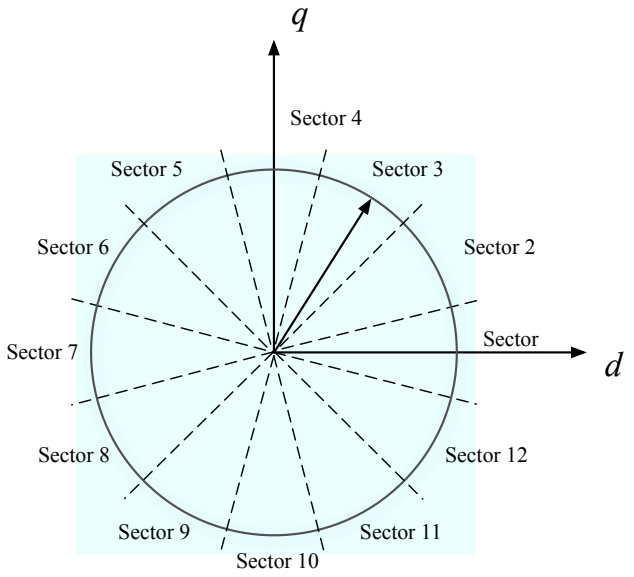

(b)

Figure 3.3: Voltage space representations and flux phasor trajectory in (a) six-step implementation and (b) 12-step implementation.

In the six-step approach, there exists a unique vector in order to advance or retard the flux angle and to simultaneously amplify the flux magnitude or attenuate the flux linkage. But this approach limits the torque and flux gains to be fixed at 70.7% V_{DC} in a sliding mode equivalent implementation.

Table 3.1: Error Bands in Switching States

$e_\phi < 0$	if	$\lvert\vec{\lambda}_s\rvert < \lvert\vec{\lambda}_{sref}\rvert - \lvert\Delta\lambda_s\rvert$
$e_\phi \geq 0$	if	$\lvert\vec{\lambda}_s\rvert \geq \lvert\vec{\lambda}_{sref}\rvert + \lvert\Delta\lambda_s\rvert$
$e_\tau < 0$	if	$T_e < T_{e,ref} - \Delta T$
$e_\tau = 0$	if	$T_e = T_{e,ref}$
$e_\tau > 0$	if	$T_e > T_{e,ref} + \Delta T$

Table 3.2: Six-Sector Switching Strategy for Conventional DTC

Sector		#1	#2	#3	#4	#5	#6
ρ	$\in$	$(-\frac{\pi}{6}, \frac{\pi}{6})$	$(\frac{\pi}{6}, \frac{\pi}{2})$	$(\frac{\pi}{2}, \frac{5\pi}{6})$	$(\frac{5\pi}{6}, -\frac{5\pi}{6})$	$(-\frac{5\pi}{6}, -\frac{\pi}{2})$	$(-\frac{\pi}{2}, -\frac{\pi}{6})$
	$e_\tau > 0$	(-1,-1,1)	(1,-1,1)	(1,-1,-1)	(1,1,-1)	(-1,1,-1)	(-1,1,1)
$e_\phi > 0$	$e_\tau = 0$	(-1,-1,-1)	(1,1,1)	(-1,-1,-1)	(1,1,1)	(-1,-1,-1)	(1,1,1)
	$e_\tau < 0$	(-1,1,-1)	(-1,1,1)	(-1,-1,1)	(1,-1,1)	(1,-1,-1)	(1,1,-1)
	$e_\tau > 0$	(1,-1,1)	(1,-1,-1)	(1,1,-1)	(-1,1,-1)	(-1,1,1)	(-1,-1,1)
$e_\phi < 0$	$e_\tau = 0$	(1,1,1)	(-1,-1,-1)	(1,1,1)	(-1,-1,-1)	(1,1,1)	(-1,-1,-1)
	$e_\tau < 0$	(1,1,-1)	(-1,1,-1)	(-1,1,1)	(-1,-1,1)	(1,-1,1)	(1,-1,-1)

The possible output voltage space is limited to eight different vectors or six different non-zero vectors. This approach results in a higher torque and flux ripple and reduced torque capability, compared to continuous flux angle implementation. The flux and torque regulation performance is inherently limited and cannot be improved via control based on six-step flux angle quantization.

Reduced torque and flux ripple can be obtained by enhancing the quantization resolution. For example, 12-step flux angle quantization provides better flux and torque regulation and reduced ripple compared to the 6-step approach. With 12-step quantization, the torque and flux gains are not limited to 70.7%, and can be increased or decreased depending on requirements. A 12-step voltage space representation and vector selection scheme is given in Fig. 3.3 and Table 3.3.

The provided discussion has been experimentally evaluated. From Fig. 3.4, it can be seen that the stator flux ripple of a particular six-sector DTC implementation (for which the rated flux is 600 mV·s) is 300 mV·s. With 12- and 256-step implementations, the flux ripple can be reduced to approximately 200 mV·s and 100 mV·s, respectively. Improved performance can be obtained with continuous flux angle implementation (as would be used in

Table 3.3: 12-Sector Switching Strategy for DTC

Sector		#1	#2	#3	#4	#5	#6
ρ	$\in$	$(-\frac{\pi}{12}, \frac{\pi}{12})$	$(\frac{\pi}{12}, \frac{\pi}{4})$	$(\frac{\pi}{4}, \frac{5\pi}{12})$	$(\frac{5\pi}{12}, \frac{7\pi}{12})$	$(\frac{7\pi}{12}, \frac{3\pi}{4})$	$(\frac{3\pi}{4}, \frac{11\pi}{12})$
$e_\phi > 0$	$e_\tau > 0$	(-1,-1,1)	(-1,1,1)	(-1,-1,1)	(1,-1,1)	(-1,-1,1)	(1,-1,1)
	$e_\tau = 0$	(-1,-1,-1)	(1,1,1)	(-1,-1,-1)	(1,1,1)	(-1,-1,-1)	(1,1,1)
	$e_\tau < 0$	(-1,1,1)	(-1,1,1)	(-1,-1,1)	(1,-1,1)	(1,-1,-1)	(1,-1,1)
$e_\phi < 0$	$e_\tau > 0$	(1,-1,-1)	(1,-1,-1)	(1,1,-1)	(-1,1,-1)	(1,1-,1)	(-1,1,-1)
	$e_\tau = 0$	(1,1,1)	(-1,-1,-1)	(1,1,1)	(-1,-1,-1)	(1,1,1)	(-1,-1,-1)
	$e_\tau < 0$	(1,1,-1)	(1,-1,-1)	(1,1,-1)	(-1,1,-1)	(-1,1,1)	(-1,1,-1)

Sector		#7	#8	#9	#10	#11	#12
ρ	$\in$	$(\frac{11\pi}{12}, -\frac{11\pi}{12})$	$(-\frac{11\pi}{12}, -\frac{3\pi}{4})$	$(-\frac{3\pi}{4}, -\frac{7\pi}{12})$	$(-\frac{7\pi}{12}, -\frac{5\pi}{12})$	$(-\frac{5\pi}{12}, -\frac{\pi}{4})$	$(-\frac{\pi}{4}, -\frac{\pi}{12})$
$e_\phi > 0$	$e_\tau > 0$	(1,-1,-1)	(1,1,-1)	(1,-1,-1)	(1,1,-1)	(-1,1,-1)	(-1,1,1)
	$e_\tau = 0$	(-1,-1,-1)	(1,1,1)	(-1,-1,-1)	(1,1,1)	(-1,-1,-1)	(1,1,1)
	$e_\tau < 0$	(1,-1,-1)	(1,1,-1)	(-1,1,-1)	(1,1,-1)	(-1,1,-1)	(-1,1,1)
$e_\phi < 0$	$e_\tau > 0$	(-1,1,1)	(-1,-1,1)	(-1,1,1)	(-1,-1,1)	(1,-1,1)	(1,-1,-1)
	$e_\tau = 0$	(1,1,1)	(-1,-1,-1)	(1,1,1)	(-1,-1,-1)	(1,1,1)	(-1,-1,-1)
	$e_\tau < 0$	(-1,1,1)	(-1,-1,1)	(1,-1,1)	(-1,-1,1)	(1,-1,1)	(1,-1,-1)

conventional FOC), since the inverter is no longer a bottleneck.

Several implementation methods are discussed here, and the effect of increased step-size is theoretically and experimentally evaluated. The results show that increasing the resolution introduces the flexibility to obtain faster torque or flux responses. From a performance perspective, continuous flux angle DTC inherently tends to choose the closest vector to the previous stator angle. Therefore, maximizing the number of vectors that is analogous to continuous flux angle, minimizes the torque and flux ripple.

3.2 Direct Torque Control Performance

Performance enhancements in the literature include improved six-step switching tables [30], comparators with two- or three-level hysteresis [31], implementation of DTC employing space-vector modulation (SVM) [31], [32], fuzzy control [33], and sophisticated flux observers [34]. Casadei et al. provide a general discussion and review on DTC and FOC [20]. Nillesen et al. implemented a predictive pulse-width control method with DTC to achieve

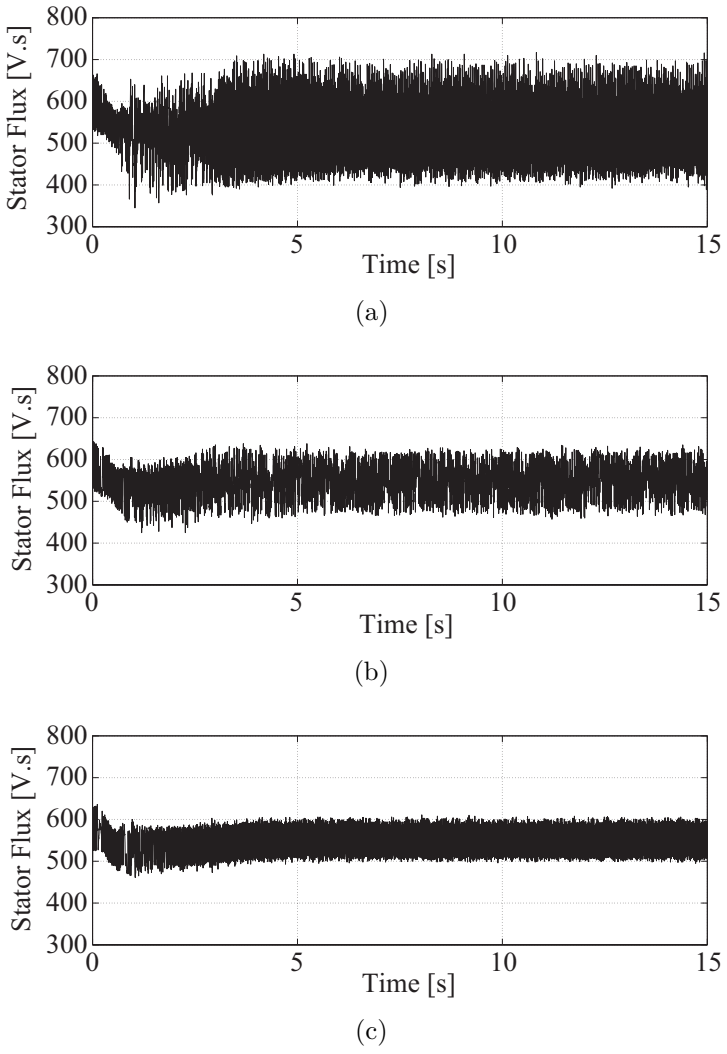

Figure 3.4: DTC stator flux regulation performances for different flux angle quantization rates. (Note the change in the vertical axes.) (a) 6-step DTC, (b) 12-step DTC, (c) 256-step DTC

satisfactory flux regulation, but the torque response did not improve [35]. This problem is linked to the stochastic nature of the shaft torque, since actual torque cannot be predicted. However, the method is also limited by six-step quantization.

Habetler et al. achieved torque control at very low speeds by employing a low-pass filter during stator voltage integration, but torque control is lost after 30 s when operating at frequencies as low as 0.3 Hz [34]. In [33], a fuzzy controller achieved constant switching frequency, low torque and current distortion; and a low sampling rate. The required structure is rela-

tively complex, a space vector modulator is required, and low sampling rates cause harmonic current distortion and steady-state torque error. Several approaches, including PI and fuzzy controllers for torque and flux regulation, adjust the torque and flux control input vectors to minimize torque and flux ripple in the system [36], [37]. These are smoother but slower than bang-bang control methods. The slower response tends to diminish the advantages of DTC. In [36] and [37], fuzzy controllers for DTC apply six-step quantization. Once again, system performance is limited by this inverter operating method.

Lee et al. presented a dead-beat type controller implemented on a SVM-DTC. The transient response and steady-state responses of the system are shown to achieve satisfactory results even at low switching frequencies, albeit with extensive sensitivity to parameter uncertainties and parameter mismatches [38]. Jezernik presented a new flux estimator approach, but it is shown that this method increases the parameter sensitivities and introduces a trade-off of parameter sensitivity and robustness [39]. The problems that can be caused due to low precision integration during stator flux estimation are addressed in [40]. A modified integrator structure embedding a high-pass filter to avoid dc drift is presented. Wan et al. implemented auto disturbance rejection control (ADRC) to DTC [41]. This method is shown to reject disturbances at the expense of extensive parameter sensitivity.

Sorchini proved that the minimum number of discrete steps required for a successful inverter process that supports DTC operation is five [6], although at least six steps are required to achieve symmetric stator voltages. A continuous stator angle approach that supports a PWM inverter would cancel ripple injection due to flux angle quantization, at least up to the selected switching frequency. The conventional link between the switching scheme and the controller is not fundamental for DTC [26].

3.3 Problem Evaluation

3.3.1 Stator Resistance Mismatches

A conventional DTC drive as shown in Fig. 2.8 requires flux angle and stator flux magnitude estimation. These quantities are estimated using (2.15) and (2.16). This flux estimation scheme introduces stator resistance dependency,

Table 3.4: Effect of Stator Resistance on Estimation Errors

$\lvert\lambda_s^e\rvert > \lvert\lambda_s\rvert$,	$\rho_s^e > \rho_s$ and	$\tau^e = \vec{\lambda}_s^e \times \vec{i}_s^e > \tau$ for	$r_s' < r_s$
$\lvert\lambda_s^e\rvert < \lvert\lambda_s\rvert$,	$\rho_s^e < \rho_s$ and	$\tau^e = \vec{\lambda}_s^e \times \vec{i}_s^e < \tau$ for	$r_s' > r_s$

which is the primary parameter sensitivity in the control structure. As explained, this method conceptually adjusts the angle between the stator and rotor fluxes. Precise position and the magnitude knowledge of the stator flux are fundamental to reliable operation. Furthermore, the estimator in (2.15) is used instead of an observer to avoid parameter sensitivities. Unlike an observer, the error in an estimator does not exponentially diminish. Therefore, any parameter mismatches from the beginning of the operation will have a performance degradation effect throughout the entire operation.

Incorrect resistor information in the estimator leads either to under- or over-estimation of the torque and flux. For example, assuming sinusoidal voltages and currents

$$\vec{v_s} = |\vec{v}_s|e^{j\theta_s}$$
$$\vec{i_s} = |\vec{i}_s|e^{j\alpha_s}$$

where θ_s and α_s are the phase angle of the stator voltage and current, respectively. The estimated stator flux will be

$$\lambda_s^e = \int_0^t v_s - i_s r_s' dt = |\lambda_s^e| e^{j\rho_s^e} \tag{3.6}$$

and the underestimated stator resistance estimate r_s' leads the estimated flux (λ_s^e), angle (ρ_s^e) and torque (τ_s^e) to be greater than the actual values as shown in Table 3.4. Likewise, an overestimated r_s' causes the estimates to be lower than the actual values. The superscript e stands for the estimation. Under incorrect stator resistance information, the system does not have the correct flux angle and the switching mode selection will not be optimal. For example, a space vector selection may decrease the generated torque instead of increasing it. Analytical derivation of this phenomenon can be demonstrated using the input voltages in a sliding mode approach.

By approximating the stator flux as

$$\rho_s^e = \rho_s + e_\rho,$$

and the transformation matrix

$$\begin{bmatrix} v_{ds} \\ v_{qs} \end{bmatrix} = \begin{bmatrix} \cos(\rho_s^e) & -\sin(\rho_s^e) \\ \sin(\rho_s^e) & \cos(\rho_s^e) \end{bmatrix} \begin{bmatrix} u_\phi \\ u_\tau \end{bmatrix}$$

the dq axes voltages to be applied can be found by

$$\begin{aligned} v_{ds} = &\cos(\rho_s)\left(u_\phi \cos(e_\rho) - u_\tau \sin(e_\rho)\right) \\ &- \sin(\rho_s)\left(u_\phi \sin(e_\rho) + u_\tau \cos(e_\rho)\right) \end{aligned} \tag{3.7a}$$

$$\begin{aligned} v_{qs} = &\cos(\rho_s)\left(u_\tau \cos(e_\rho) + u_\phi \sin(e_\rho)\right) \\ &- \sin(\rho_s)\left(u_\tau \sin(e_\rho) - u_\phi \cos(e_\rho)\right). \end{aligned} \tag{3.7b}$$

Assuming zero stator resistance, the stator flux linkage can be expressed as

$$\vec{V_s} = \frac{d}{dt}\vec{\lambda_s} = j|\vec{\lambda_s}|\frac{d\rho_s}{dt}, \tag{3.8}$$

where e_ρ denotes stator flux estimation error. From (3.9), it can be seen that the decoupling between torque and flux commands is compromised. The torque command is inside the flux regulation loop and vice versa.

The stator resistance sensitivity of the electromagnetic torque is investigated. The fast reduced model (2.12) shows that the steady-state torque expression is found as

$$\tau = -\frac{n_p}{\gamma}\omega\phi + \frac{1}{\gamma}\sqrt{\phi}u_\tau. \tag{3.9}$$

Drawing notation from [13, 26], the sensitivity of electromagnetic torque to stator resistance can be found as

$$\Delta\tau = J_{r_s}\Delta r_s,$$

and the jacobian is computed as

$$J_{r_s} = \frac{\partial\tau}{\partial r_s} = \frac{n_p\omega\phi}{\gamma^2} - \frac{1}{\gamma^2}\sqrt{\phi}u_\tau. \tag{3.10}$$

Keeping this in mind, the jacobian can be rewritten as

$$J_{r_s} = -\frac{1}{\gamma}\tau. \tag{3.11}$$

Using the definition of differentiation in (3.13),

$$\lim_{\Delta t \to 0} \frac{\Delta \tau}{\Delta t} = -\lim_{\Delta t \to 0} \frac{1}{\gamma}\tau \frac{\Delta r_s}{\Delta t} \tag{3.12}$$

$$\frac{d\tau}{dt} = -\frac{1}{\gamma}\tau \frac{dr_s}{dt}, \tag{3.13}$$

can be found. Equation (3.15) shows that an increment in stator resistance during the operation does not affect the stability, and the torque response converges to references in finite time. On the other hand, a decrement in the stator resistance might cause the eigenvalues to be on the right-hand side of the complex plane, hence causing unstable operation.

From Fig. 3.5, the effect of increased stator resistance in the torque regulation can be observed. The torque oscillations attenuate and electromagnetic torque converges to the reference value. As the rate of change increases, the system dynamics require more time to damp the oscillations. On the other hand, Fig. 3.6 shows that a decrement in the stator resistance results in a completely unstable system. Therefore, this study justifies the conclusion that correct stator resistance is imperative for reliable system operation. This phenomenon is also discussed by Lee and Krishnan [42] without any analytical study.

3.3.2 Torque-Speed Coupling

Common drive systems often utilize flux weakening in order to attain operation beyond rated speed. However, this introduces a trade-off between torque capability and operating speed range. The steady-state torque expression obtained from the slow reduced model

$$\tau = -\frac{n_p}{\gamma}\omega\phi + \frac{1}{\gamma}\sqrt{\phi}u_{\tau,slow}, \tag{3.14}$$

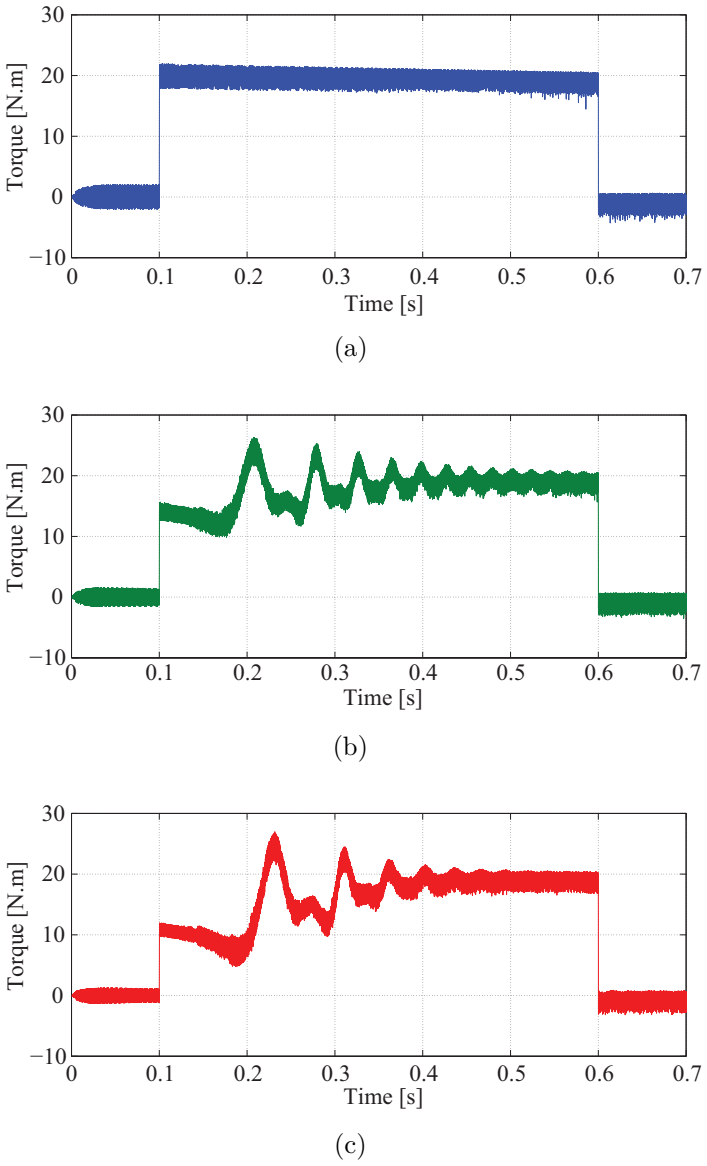

Figure 3.5: Induction machine DTC torque output with (a) no variation in stator resistance, (b) 25% increase in stator resistance, and (c) 50% increase in stator resistance.

shows that under field weakening (decrease in $\sqrt{\phi}$), the effective sliding mode control gain reduces. From the fast reduced model, dynamic torque response is compromised. In addition, (3.16) suggests that maximum torque capability also reduces as rotor speed increases. Thus, torque is directly coupled to rotor speed and stator flux linkage.

This problem is experimentally demonstrated on a 3/4 HP, 3-ϕ induction motor with 240 V rated stator voltage and a rated flux of 0.6 V·s in Fig. 3.7.

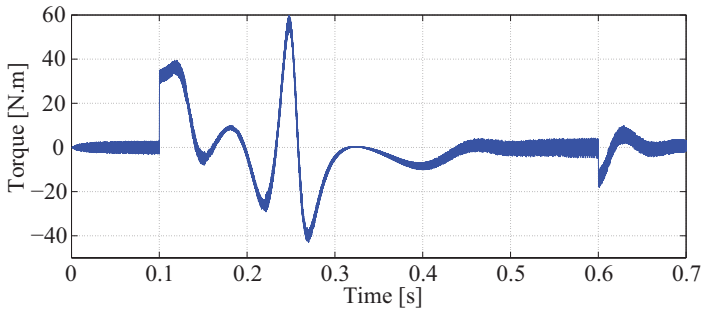

(a)

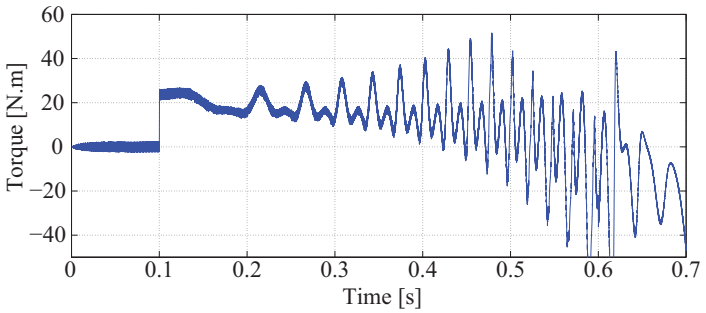

(b)

Figure 3.6: Induction machine DTC torque output with (a) 25% decrease in stator resistance, (b) 10% decrease in stator resistance.

This implementation uses a PWM inverter with continuous stator flux angle. Stator flux is fixed at 550 mV·s. The system runs the machine up to 2200 RPM counter-clockwise under a 0.15 N·m load torque. A clockwise torque command of 0.5 N·m is then applied. Due to the coupling between speed and torque, the shaft torque of the machine exponentially decays to 0.2 N·m as the rotor speed increases in the clockwise direction. Compensation methods for this inherent sensitivity of torque capability on rotor speed and stator flux are presented in detail within Section 3.4.

3.4 Compensation Approaches

This section is a compilation of material previously published in [43]. The fast reduced model can provide insight for enhancing torque performance under DTC. Rotor speed sensitivity of the electromagnetic torque can be reduced by introducing speed feedback into the torque command. However,

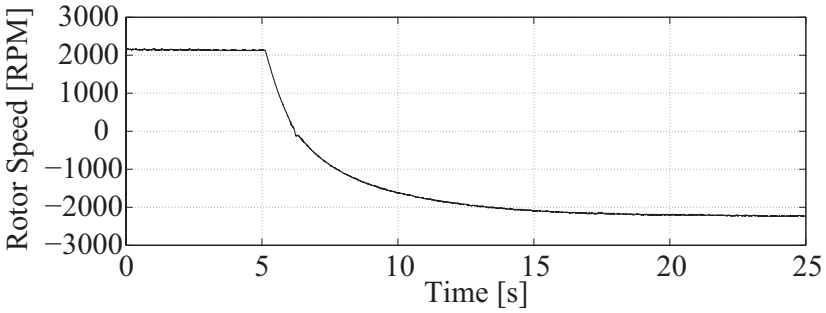

(a)

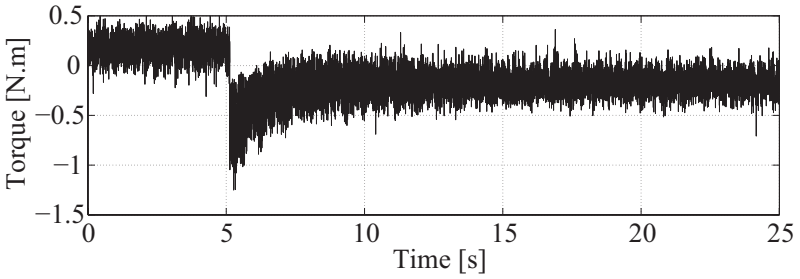

(b)

Figure 3.7: Induction machine DTC drive problem evaluation. (a) Rotor speed in revolutions per minute, (b) electromagnetic torque in N·m.

the reduced model will not be accurate for a high-leakage machine. The effective torque gain can be obtained as

$$k'_\tau = \frac{\phi - \sigma\eta}{\sqrt{\phi} L_s} k_\tau. \tag{3.15}$$

This shows that, with a non-zero leakage factor, the effective torque gain of the system reduces as η increases. A correction term for high-leakage machines can be employed for compensation.

3.4.1 Input-Output Decoupling

Input-output decoupling (IOD) was discussed for the exponentially stable DTC approach presented in [6, 27]. Compensated inputs for low- or high-leakage machines become

$$u_\tau = \frac{\gamma\tau + n_p\omega\phi}{\sqrt{\phi}} - k_\tau sgn(\tau - \tau_{ref}) \tag{3.16}$$

and

$$u_\tau = \frac{(\gamma\tau + n_p\omega\phi)L_s - \phi k_\tau sgn(\tau - \tau_{ref})}{\phi - \sigma\eta}. \tag{3.17}$$

These feedback structures enhance torque dynamics at the expense of complexity and sensors.

The dynamic torque equation in the fast time scale becomes

$$\frac{d\tau}{dt_f} = \frac{1}{L_s}\sqrt{\phi}u_\tau. \tag{3.18}$$

The required torque gain is relatively small since other effects have been compensated out. Notice that this method is susceptible to noise and requires full state feedback to achieve precise decoupling. In contrast to conventional DTC, robustness is foregone in exchange for decoupled performance. However, any extra voltage headroom required to implement this decoupling method reduces headroom required for flux and torque regulation and could limit system response.

3.4.2 Asymptotic Input-Output Decoupling

Asymptotic input-output decoupling (AIOD) can be used in order to avoid issues regarding torque and flux ripple injection, computational complexity and parameter sensitivity. Given sufficient inverter voltage, DTC will converge within a hysteresis band. The fundamental idea is to use the commanded torque and flux values in place of state values. AIOD can be formulated as

$$u_\tau = \frac{\gamma\tau_{ref} + n_p\omega\phi_{ref}}{\sqrt{\phi_{ref}}} - k_\tau sgn(\tau - \tau_{ref}) \tag{3.19}$$

for low-leakage machines and

$$u_\tau = \frac{(\gamma\tau_{ref} + n_p\omega\phi_{ref})L_s - \phi_{ref}k_\tau sgn(\tau - \tau_{ref})}{\phi_{ref} - \sigma\eta} \tag{3.20}$$

for high-leakage machines. The dynamic torque equation becomes

$$\sigma\frac{d\tau}{dt_f} = -\frac{\gamma}{L_s}e_\tau - \frac{n_p}{L_s}\omega e_\phi - \frac{1}{L_s}\sqrt{\phi}k_\tau sgn(e_\tau). \tag{3.21}$$

The stability of this method can be investigated by defining a Lyapunov function based on squared error and its derivative,

$$\begin{aligned} V &= \frac{1}{2}e_\tau^2 + \frac{1}{2}e_\phi^2 \\ \dot{V} &= -\dot{e_\tau}e_\tau - \dot{e_\phi}e_\phi \\ &= -\dot{\tau}e_\tau - \dot{\phi}e_\phi \\ &= -\frac{2r_s r_r}{\gamma L_r}\phi e_\phi - 2\sqrt{\phi}\left(\frac{\gamma - r_s}{\gamma}\right)k_\phi|e_\phi| \\ &\quad - \frac{\gamma}{L_s}e_\tau^2 - \frac{n_p}{L_s}\omega e_\phi e_\tau - \frac{1}{L_s}\sqrt{\phi}k_\tau|e_\tau|. \end{aligned} \tag{3.22}$$

By defining bounds on the controllers gains,

$$\begin{aligned} k_\phi &\geq \frac{r_s L_r}{L_s}\sqrt{\phi_{sat}} \\ k_\tau &\geq \frac{n_p\omega}{\sqrt{\phi_0}}\max[e_\phi] \\ &\geq \frac{n_p\omega}{\sqrt{\phi_0}}|\phi_{sat} - \phi_0| \end{aligned}$$

and choosing the controller gains, k_ϕ and k_τ,

$$k_\phi = \frac{r_s L_r}{L_s}\sqrt{\phi_{sat}} + \delta_\phi \tag{3.23a}$$

$$k_\tau = \frac{n_p\omega}{\sqrt{\phi_0}}|\phi_{sat} - \phi_0| + \delta_\tau, \tag{3.23b}$$

the stability of the system can be guaranteed. This holds since persistent switching will excite non-zero error. For $\delta_\phi > 0, \delta_\tau > 0$, the Lyapunov function derivative becomes

$$\begin{aligned} \dot{V} &= -2\sqrt{\phi}\left(\frac{\gamma - r_s}{\gamma}\right)\delta_\phi|e_\phi| \\ &\quad - \frac{\gamma}{L_s}e_\tau^2 - \frac{1}{L_s}\sqrt{\phi}\delta_\tau|e_\tau| \\ &\leq 0, \end{aligned}$$

which satisfies stability conditions. Comparing gain limits established for AIOD with those for conventional DTC presented in [6], the AIOD method relaxes the controller gain requirements and provides high performance with smaller controller gains.

Using the controller gain boundaries presented in [6], the overall voltage headroom change in AIOD implementation is

$$\Delta u = \frac{\gamma}{\sqrt{\phi}}(\tau_{max} - \tau_{ref}) - \frac{n_p \omega}{\sqrt{\phi_0}}(\phi_{ref} - \phi_0). \tag{3.24}$$

For a negligible γ value, this means the overall voltage headroom is reduced.

The AIOD method reduces the defined boundaries on the flux and torque controller gains, yet also reduces the overall headroom for torque regulation. Combined with reduced controller gains, the torque regulation will be slowed at high speeds. However, without such a compensation approach, stability at high speeds cannot be achieved with conventional DTC drives. The AIOD approach supports a wider operating speed range for DTC induction machines.

3.5 Results

The AIOD method has been implemented experimentally on a 3/4 HP, three phase, 230 V, four-pole symmetrical squirrel cage induction machine and compared to conventional DTC. Figure 3.8 demonstrates speed reversal performance of AIOD implemented with a PI controller. The torque controller gain is lower than in conventional DTC. Figure 3.8(b) shows that torque regulation is slower for AIOD than for conventional DTC.

Figures 3.9 and 3.10 demonstrate operation up to 200 rad/s. Conventional DTC is driven to 200 rad/s, then the shaft torque is increased step by step. The system provides near-ideal operation up to about 0.1 N·m at the given speed. Because of speed coupling, increasing load steps slow the machine down. When load torque reaches 0.8 N· m at $t = 16$ s, the machine stalls. Figure 3.10 shows speed performance under AIOD for the same load steps. Regulation is nearly ideal except at the transition times. Figure 3.10 (b) shows that 1.2 N·m of torque can be supported at 200 rad/s and rated current.

Maximum rotor speeds under field weakening are presented in Figure 3.11. Here a high constant torque is commanded and rotor speeds are measured for various stator fluxes. The motor base speed is 1500 RPM at 50 Hz. Figure 3.11(a) shows that AIOD can achieve 3500 RPM when flux is reduced to 250 mV·s. At $t = 32$ s, the rotor speed drops to 3200 RPM and attempts to

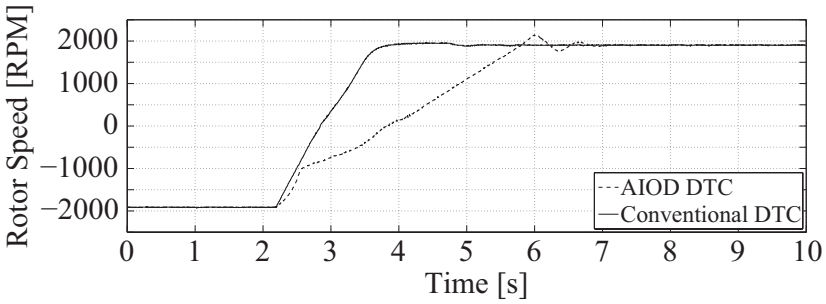

(a)

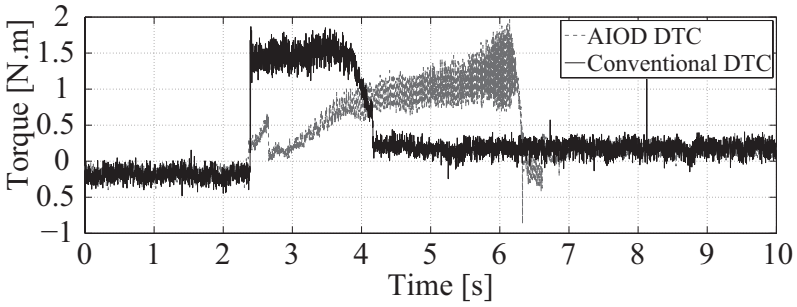

(b)

Figure 3.8: Induction machine conventional and AIOD DTC performance under speed reversal. (a) Rotor speed RPM, (b) torque in N·m.

recover. The dip is because at speed ratings more than twice the base speed, voltage headroom shrinks to 50% of that at base speed. The torque gain of the system together with the feedback reaches the voltage limitation. This causes the sliding mode controller to lose control briefly, leading to disturbances at the maximum speed. Figure 3.11 (b) shows that in conventional DTC a maximum speed of 2700 RPM is achieved with 300 mV·s stator flux (half of the rated value). Further field weakening results in stall.

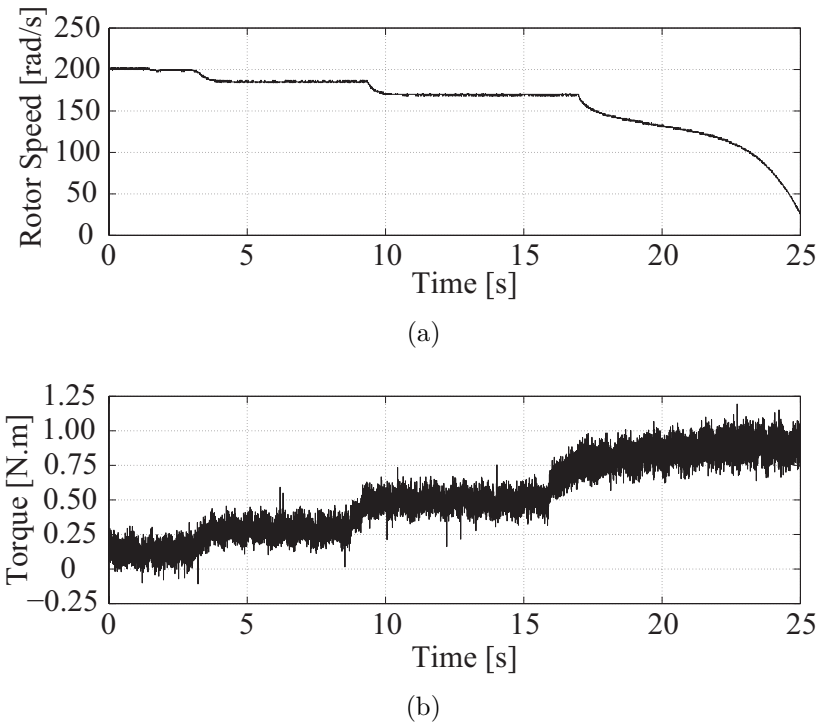

Figure 3.9: Conventional DTC drive load test. (a) Rotor speed in rad/s, (b) torque in N·m.

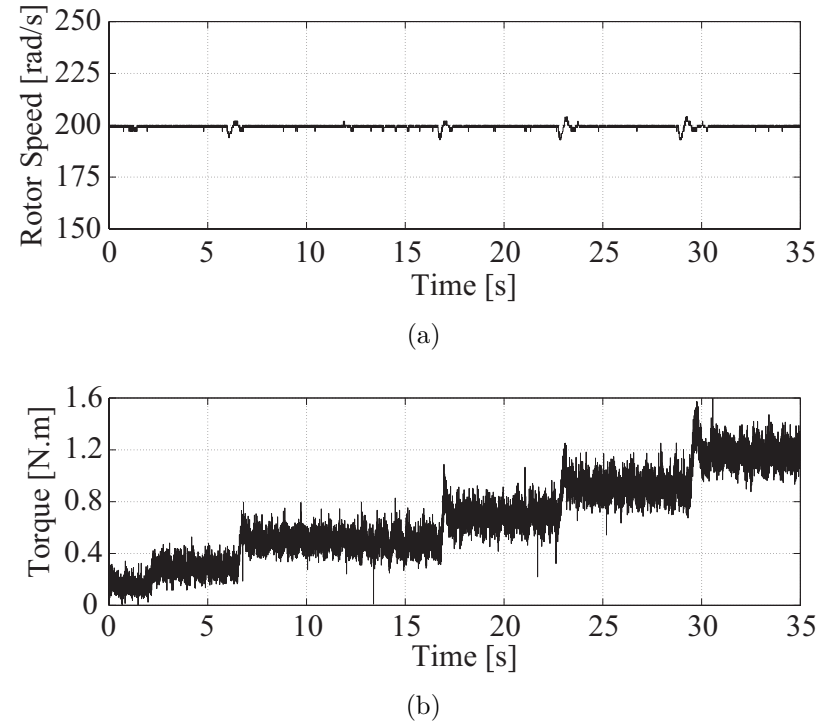

Figure 3.10: AIOD load test. (a) Rotor speed in rad/s, (b) torque in N·m.

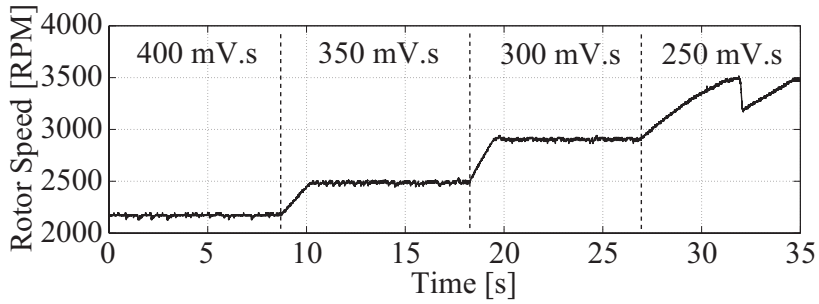

(a)

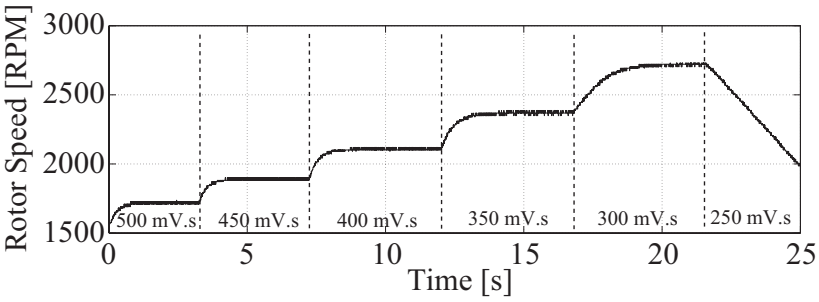

(b)

Figure 3.11: Induction machine maximum speed investigation. (a) AIOD, (b) conventional DTC.

CHAPTER 4

DRIVE SYSTEM MAXIMUM INSTANTANEOUS TORQUE CAPABILITIES

This chapter is a compilation of material previously published in [44]. Drives designers in the literature have focused on the steady-state capabilities of an induction machine. Instantaneous capabilities, which are only limited by thermal capabilities and magnetic saturation, are the topics of this chapter. The volts-per-hertz (V/f) method controls only the stator frequency to be applied to a machine and sets the stator flux to a constant value associated with a certain V/f ratio. Because it does not use the entire voltage headroom, the peak torque capability is inherently limited. To demonstrate this limitation, a comparative peak torque capability analysis of V/f control and two well-known vector controllers, DTC and FOC, is presented. The results show that the vector controllers enhance peak torque by employing the entire voltage headroom while simultaneously avoiding saturation.

How do existing vector controllers, such as FOC and DTC, limit the available voltage headroom for torque generation and still provide superior torque capabilities and response? The FOC strategy decouples the torque and rotor-flux generating components of the stator current via feedback, thus achieving decoupling [2]. It has been shown that the torque response of FOC can be improved with much less control effort [25] by using stator [24] or air-gap [23] flux linkages instead of rotor fluxes. The DTC strategy emphasizes the importance of the stator flux angle to obtain fast torque response [3]. It uses a limit-cycle control to advance or retard the stator flux phase angle to enable instantaneous response [7].

Maximum torque control and maximum torque per ampere (MTA) control strategies have been investigated and applied to motor control methods including V/f control and FOC [16, 17, 18, 19]. The analysis shows that maximum torque per stator current is achieved with a 45° lag between stator voltages and currents. The results associated with the method proposed in this thesis show that a 46.4° lag between stator voltages and currents

is achieved while maximizing the instantaneous torque. MTA is employed in steady-state applications. Usually the stator currents are constrained to rated values. In contrast, the proposed method is intended for short-term or momentary applications, allowing relaxed constraints on stator currents – less useful in steady state because of thermal limitations.

4.1 Problem Definition

Given that past work is focused on induction machine steady-state torque, how can known control strategies deliver the highest possible transient torque? The torque limit based on the steady-state torque-speed characteristic of a sample induction machine is given in Fig. 4.1(a). Ratings of the sample machine are 460 V, 3-ϕ, 10 HP, 40 A with a rated flux of 0.7 V·s. Area I corresponds to flux weakening, enforcing a stator voltage limit. Area II corresponds to the constant torque region at rated flux. The transition point is the *base speed*. Below that speed, voltage headroom is available to increase stator current. If some method could use this headroom, in principle the torque limit would approach Fig. 4.1(b). However, increasing the V/f ratio is insufficient, as this would saturate the magnetic core.

How might the voltage headroom be used to produce high short-term torque, and is the extra capability available under known control methods? To answer these questions, it is useful to evaluate the maximum torque capabilities of FOC and DTC.

4.1.1 Field-Oriented Control

As explained in Chapter 2, FOC enforces (2.9) to the stator to decouple the torque and rotor flux. It can be seen from (2.9) that both v_{ds} and v_{qs} have dependence on rotor fluxes and are supposed to be high at high rotor speeds. But the inverter stage is limited with the supplied bus voltage. Therefore, the voltage headroom is limited at high speeds and the torque capability is expected to be altered.

In principle, a user can set the flux to the rated value, then use all remaining voltage headroom to drive as high a current as possible to maximize torque. This problem is formulated as a numerical nonlinear static optimiza-

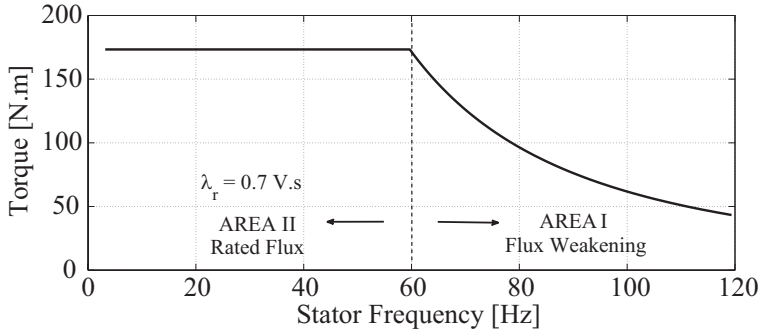

(a)

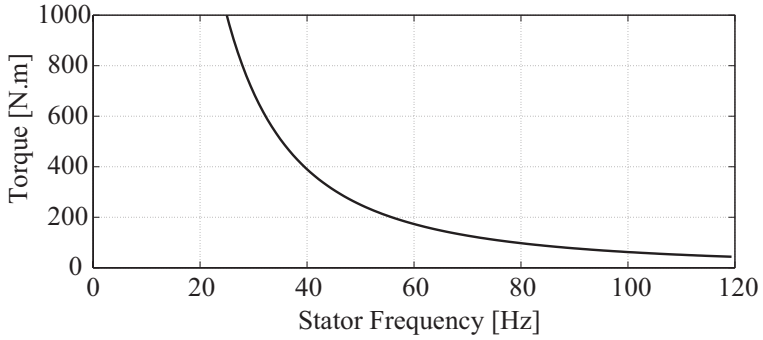

(b)

Figure 4.1: (a) Steady-state breakdown torque-speed curve under thermal and magnetic limitations and (b) torque-speed curve for linear magnetic circuit and unconstrained thermal capability.

tion problem in *Mathematica* with an objective function of

$$T_e = \frac{3}{2}\frac{n_p L_m}{L_r}(\lambda_{dr} i_{qs} - \lambda_{qr} i_{ds}), \tag{4.1}$$

and the constraints

$$\sqrt{v_{ds}^2 + v_{qs}^2} = v_{lim}$$
$$\sqrt{\lambda_{dr}^2 + \lambda_{qr}^2} \leq \lambda_{sat}.$$

To maximize torque while enforcing physical limits, the command input u_{flux} is set to achieve rated rotor flux. Then the torque command, u_{speed}, is set as high as possible subject to the voltage limit.

4.1.2 Direct Torque Control

The input commands for the sliding mode control equivalent of DTC was presented in Chapter 2. The analysis shown here focuses on continuous flux angle DTC, since limiting the output voltage vector to six possible states changes the maximum achievable RMS of the output voltage at fundamental frequency. A continuous flux angle implementation for torque and flux regulation can be seen in (2.13) and (2.14). With these in mind, the physical input voltage magnitude to be applied to the machine terminals is

$$\begin{aligned} |v_{in}| &= \sqrt{u_\phi^2 + u_\tau^2} \\ &\leq \sqrt{k_\tau^2 + k_\phi^2} \end{aligned}$$

To maintain system stability under DTC, lower bounds on torque and flux controller gains are enforced [6]. The maximum possible torque gain, in turn, is limited due to the lower bound on flux gain. These limits reduce voltage headroom for peak torque, although the instantaneous capability is still well above the steady-state limit. The electromagnetic torque expression (4.1) is maximized for a given torque and flux by constraining the stator voltages and fluxes to be

$$\begin{aligned} \sqrt{k_\tau^2 + k_\phi^2} &= v_{lim} \\ \sqrt{\phi} &\leq \lambda_{sat}. \end{aligned}$$

4.1.3 Maximum Torque Capabilities

The maximum torque capabilities of the sample induction machine under FOC for various rotor fluxes are shown in Fig. 4.2(a). Rated flux can support momentary stall torques greater than 300% of the conventional steady-state maximum torque limit. Figure 4.2(a) also demonstrates that rotor flux must be reduced to provide substantial torque capability at high speeds. In order to investigate the maximum possible torque that can be supplied by an induction machine under FOC, the rotor flux is kept at the rated value below a critical speed. This speed is defined as the operating point where a small change in the rotor flux has no effect on the torque capability. Above this speed, rotor flux should be reduced to improve the peak torque capability

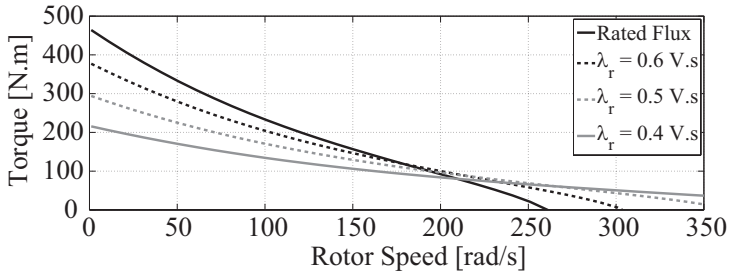

(a)

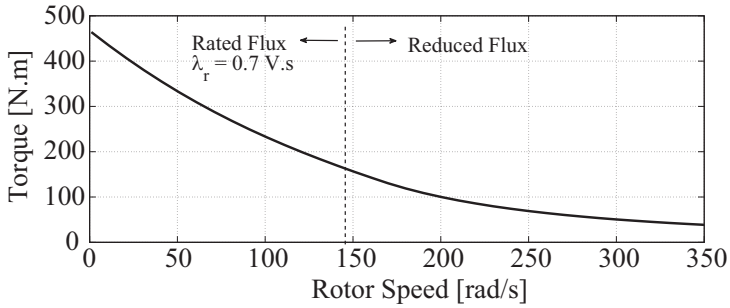

(b)

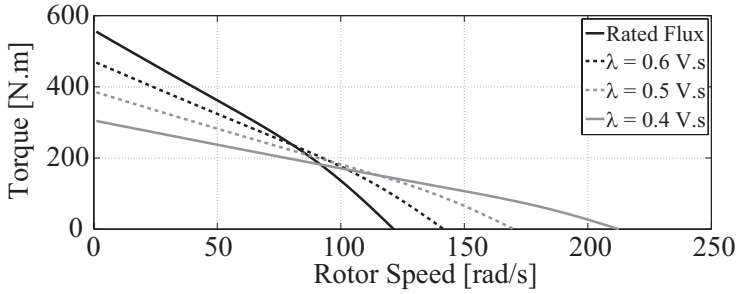

(c)

Figure 4.2: (a) Torque-speed curves of an FOC drive for certain rotor fluxes, (b) torque-speed curves of an FOC drive for certain rotor fluxes, and (c) maximum possible torque that the machine can provide under FOC.

as can be seen from Fig. 4.2(b). This critical speed can be defined as the solution to

$$\left.\frac{dT_e}{d\lambda}\right|_{\omega=\omega_c} = 0 \tag{4.2}$$

for ω_c. This condition is analogous to the field weakening regime, but here for instantaneous torque rather than continuous torque capability. In general, the critical speed is not the same as the steady-state base speed.

The maximum torque capabilities of an induction machine under DTC

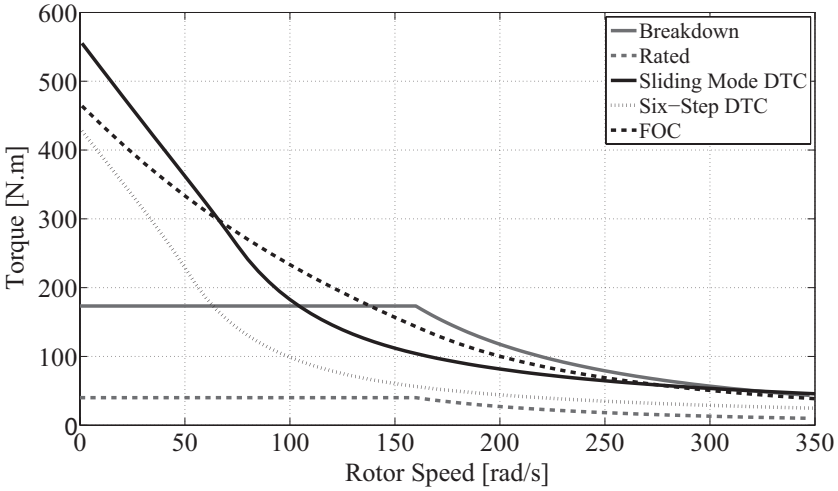

Figure 4.3: Peak torque capability comparison of sliding mode DTC, FOC, six-step DTC, steady-state breakdown torque and steady-state rated torques of the sample machine.

with different stator fluxes are shown in Fig. 4.2(c). From the figure, it can be seen that the torque capability of DTC drops off more steeper than for FOC as rotor speed increases. This result is consistent with the reduced torque capability phenomenon reported by practitioners [45]. A critical speed analysis as in (4.2) can be applied to DTC. A comparison of the absolute maximum torque that can be supplied by an induction machine under FOC, continuous flux angle DTC, and six-step DTC is shown in Fig. 4.3. The results show, for example, that the maximum torque capability of DTC can be improved by increasing flux angle quantization resolution.

The torque capability of DTC can be extended further by using PI or fuzzy controllers in the torque and flux loops, such that the torque controller gain will no longer be limited by the flux controller gain. However, the system torque and flux response speeds will be limited by the control loops used.

4.2 Augmented V/f Control

The high momentary stall torques obtained under FOC and DTC are associated with specific stator voltages and currents. Figure 4.4 shows the stator voltages and currents observed under FOC for zero speed, rated flux, and maximum torque. Rated voltage is applied at approximately 26 Hz. The

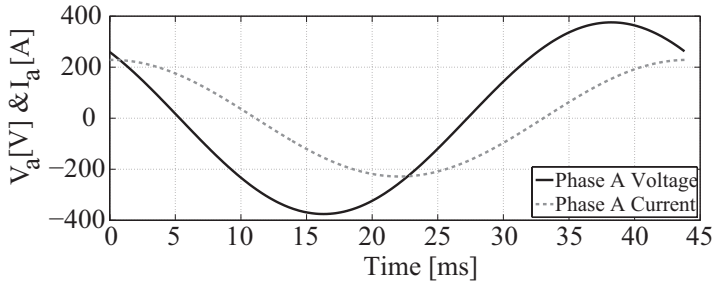

Figure 4.4: Augmented V/f controller voltages and currents at stall.

current is approximately 400% of the rated value and is lagging by 46.4° – close to the 45° lag expected under MTA control.

It should be possible to deliver the same voltages with an augmented scalar drive. For example, a look-up table for voltage magnitude and stator frequency values can be developed and used to produce high instantaneous torques with a scalar control structure. This process is unambiguous under stall conditions, as a symmetric smooth rotor can be excited based on any phase arrangement.

However, a magnitude and frequency look-up table may not yield high momentary torque. The extra voltage that drives high stator current must be orthogonal to flux control to avoid saturation; therefore phase matters. This implies that rotor position and instantaneous voltage phase must be known in order to deliver high instantaneous torque, which can be achieved using a speed encoder. Thus, with a look-up table, a vectorized V/f control, as in [21], can enforce orthogonality to yield high instantaneous torques.

Comparison of DTC and FOC provides insight into two different implementations. From Fig. 4.3, it can be seen that a continuous flux angle DTC provides high torque capability at low speeds and FOC provides high torque capability at high speeds. A DTC-based look-up table would be preferred at low speed and an FOC-based look-up table would be superior at high speed.

4.2.1 DTC-Based Augmentation Scheme

A standard DTC implementation requires two control loops – flux and torque. An augmentation scheme based on DTC must be able to keep the machine from saturating and simultaneously support the physical torque limits of the machine. This implies that either a flux regulation loop or a predictive

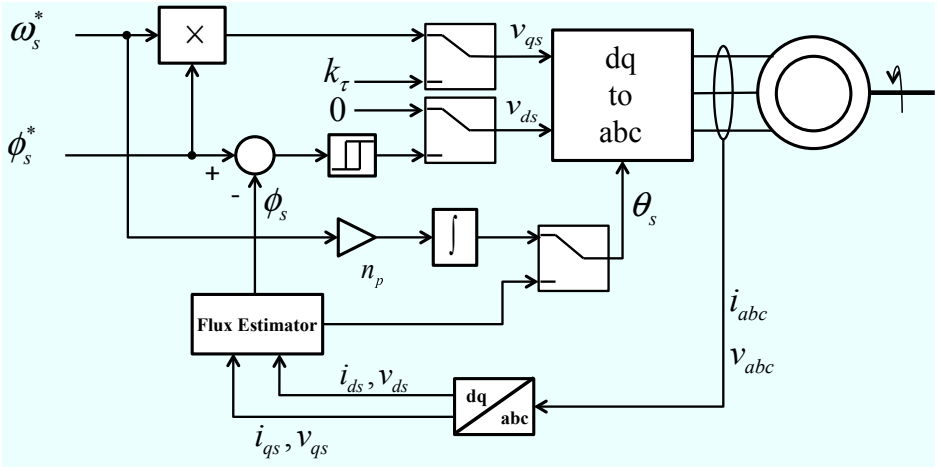

Figure 4.5: DTC-based augmentation method equivalent block diagram.

method based on rotor speed and stator currents is required to adjust the flux command u_ϕ. On the other hand, torque command u_τ of the drive can be obtained by enforcing a positive definite error manifold in (2.13). Such a method, rather than using a hysteresis torque loop, both reduces system complexity and allows the machine's physical bounds to be the only limit to the extracted torque.

Torque and flux commands are insufficient to augment the controller. From the analysis introduced in [7], DTC achieves instantaneous torque response by advancing the stator flux angle. This implies that for non-zero rotor speeds, the stator flux angle must be known. This angle can be obtained by two different approaches. One is to implement a stator flux estimator in the stationary reference frame. Another is to compute an approximate electrical slip frequency and combine it with the electrical rotor speed. Then the stator angle can be obtained by integration over time as in

$$\theta_s = \int_0^t (\frac{k_\tau L_s r_r}{\gamma L_r \phi_{ref}} + \frac{r_s}{\gamma} n_p \omega_r) dt + \theta_0. \tag{4.3}$$

Such an implementation is equivalent to Fig. 4.5. Here ω_r, θ_s, and θ_0 are the rotor mechanical speed, stator angle, and rotor initial position, respectively.

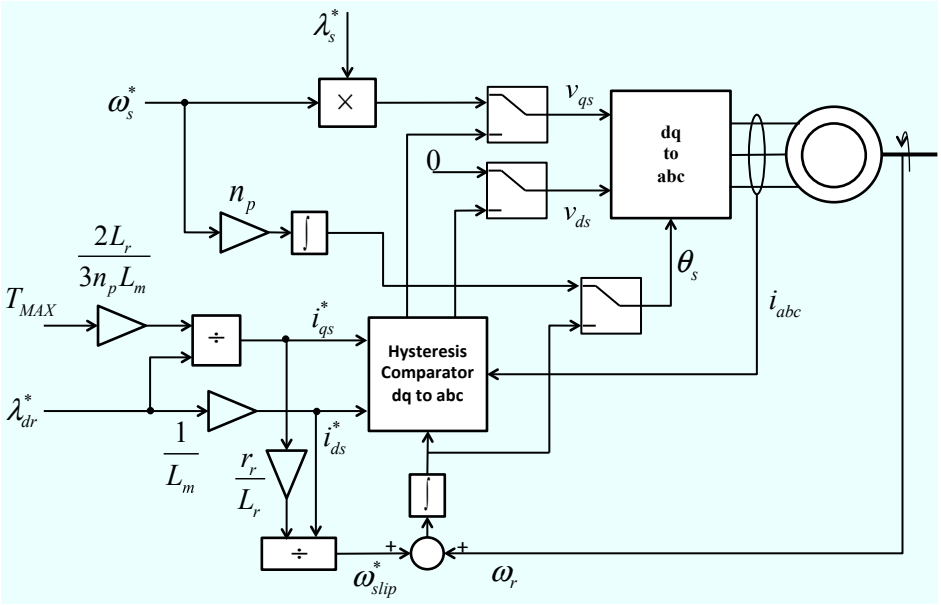

Figure 4.6: IFOC-based augmentation method equivalent block diagram.

4.2.2 FOC-Based Augmentation Scheme

In FOC augmentation, the flux command input u_{flux} is computed for a given rotor flux reference and the speed command input u_{speed} is computed from the optimization approach presented in Section 4.1.1. Using the optimized u_{speed} and u_{flux} in (2.9) , a look-up table of impressed stator currents or voltages can be generated. An implementation involving a current look-up table is analogous to an indirect-field-oriented control (IFOC) augmentation scheme, whereas a voltage look-up table method is similar to direct field-oriented control (DFOC). The stator angle can be estimated as

$$\theta_s = \int_0^t (n_p\omega_r + \omega_{slip})dt + \theta_0 \tag{4.4}$$

where ω_{slip} is the electrical slip frequency. An equivalent representation of an IFOC-based augmentation approach is given in Fig. 4.6. Simulation results provided in Fig. 4.7 show that a look-up table provided for v_{ds}, v_{qs} and ω_{slip} is sufficient to improve the peak torque capability. Figure 4.7(b) shows that augmented V/f extracts a peak transient torque that is approximately four times that of conventional V/f.

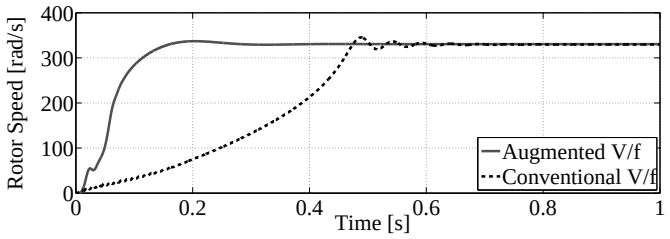

(a)

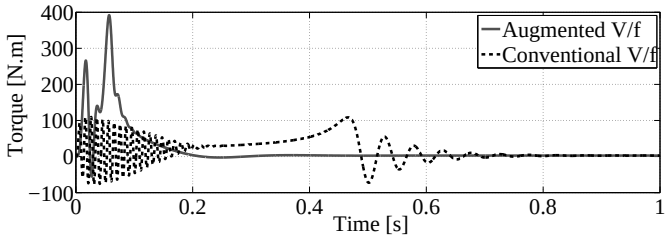

(b)

Figure 4.7: (a) Rotor speed comparison of conventional and augmented V/f control methods and (b) electromagnetic torque comparison.

4.3 Experimental Results

The described FOC-based and DTC-based augmented scalar control methods have been implemented on a 3/4 HP, three-phase, 230 V, four-pole symmetrical squirrel cage induction machine. The experimental evaluation demonstrates the torque capability at various operating speeds. Note that, in order to avoid large current spikes, the maximum output voltage is limited to 120 V. Under this condition, the rated current limits the torque at 1.4 N·m. Figure 4.8 demonstrates the response of a DTC-based augmented scalar controller at an initial speed of 50 rad/s. The system is commanded to produce maximum torque at $t = 0.6$ s, and the machine response is observed to be 1.75 N·m. After $t = 1.05$ s, the controller is switched back to conventional V/f control, resulting in rapid slowing.

Figure 4.9 provides a similar demonstration at an initial rotor speed of 150 rad/s. The system is commanded to provide maximum torque at $t = 0.48$ s, and the produced torque is observed to be 1.6 N·m. The torque response given in Fig. 4.9(b) demonstrates that as the machine speed increases above the critical speed defined in (4.2), the torque capability of the machine reduces, confirming the results presented in Fig. 4.3(c).

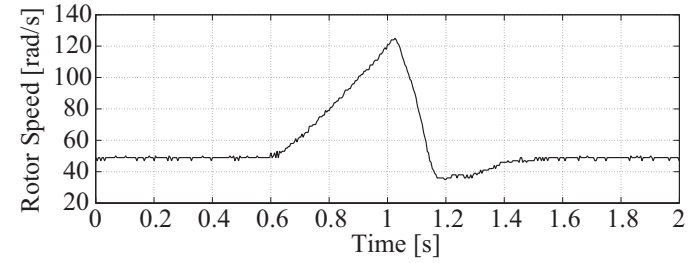

(a)

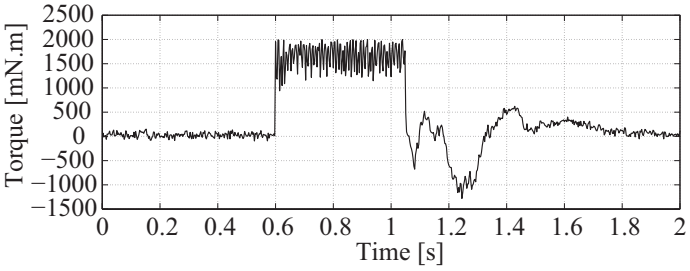

(b)

Figure 4.8: Induction machine instantaneous torque response test at 50 rad/s under DTC-based augmentation method. (a) Rotor speed and (b) torque.

IFOC-based augmentation method performance evaluations are presented in Figs. 4.10 and 4.11. In Fig. 4.10, the initial rotor speed is 50 rad/s and the machine is commanded to maximize the torque at $t = 0.6$ s. The response shows that 1.3 N·m is generated. It can also be seen that as the machine approaches the critical speed (at $t \approx 0.9$ s), the torque capability is inhibited. Figure 4.11 demonstrates the maximum torque capability of IFOC at 150 rad/s. The torque response of the machine is limited to 1.2 N·m.

It can be seen that the DTC-based augmentation scheme produces higher torques at lower speed ranges. However, as the rotor speed increases, the peak torque capability reduces rapidly. The peak torque capability of the DTC-based augmentation scheme at lower speeds is superior to the IFOC-based augmentation scheme, as predicted in Section 4.1.3.

Fig. 4.12 demonstrates the currents and voltages of a DTC-based augmented scalar controller at an initial speed of 50 rad/s. This figure presents two different transients and a steady-state operating region for the machine. The system is commanded to produce maximum torque at $t = 0.22$ s, and the machine entered the first transient region. It is seen that the augmentation method applies the overall voltage headroom to maximize the output torque.

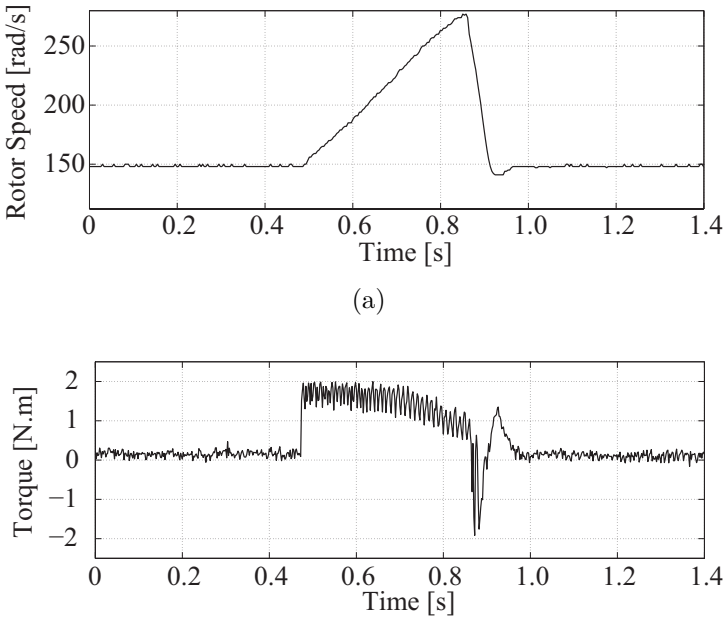

Figure 4.9: Induction machine instantaneous torque response test at 150 rad/s under DTC-based augmentation method. (a) Rotor speed and (b) torque.

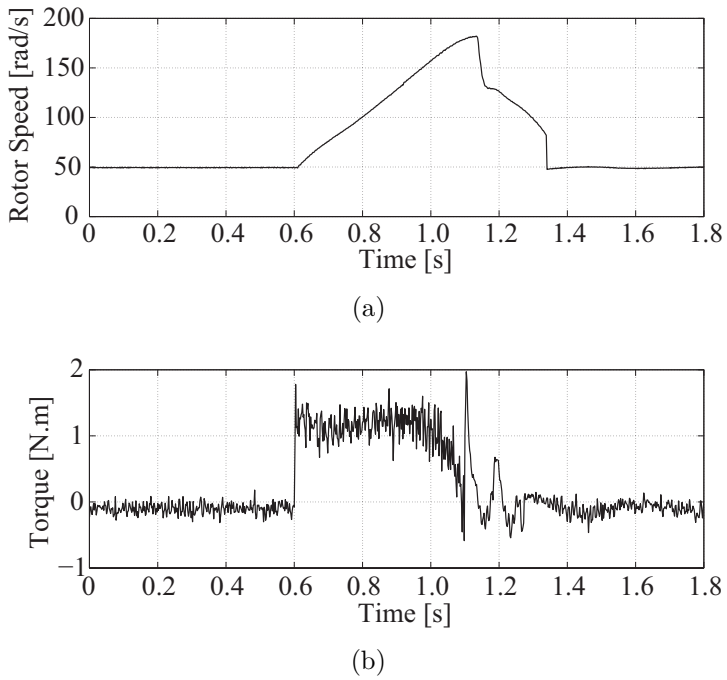

Figure 4.10: Induction machine instantaneous torque response test at 50 rad/s under IFOC-based augmentation method. (a) Rotor speed and (b) torque.

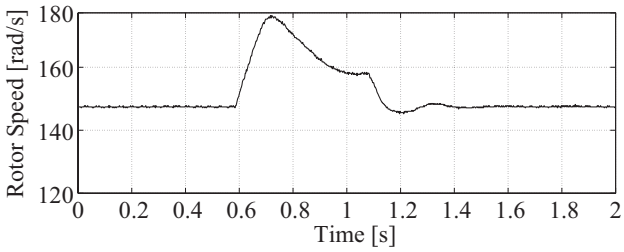

(a)

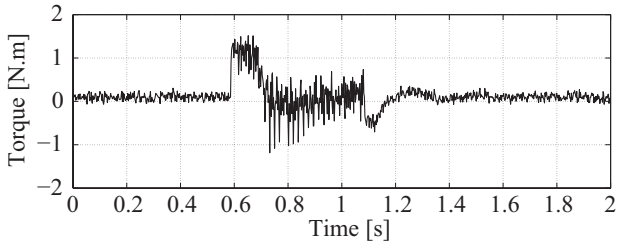

(b)

Figure 4.11: Induction machine instantaneous torque response test at 150 rad/s under IFOC-based augmentation method. (a) Rotor speed and (b) torque.

This results in a current transient shown in Fig.4.13(a). The augmentation method is turned off and conventional scalar control is activated at $t = 0.61$ s. At this time instant, the system enters the second transient region, where the machine speed goes down to 50 rad/s. This transition can be seen in Fig. 4.14. Figure 4.15 shows the transition to steady-state operation.

Similarly, Fig. 4.16 demonstrates the currents and voltages of an IFOC-based augmented scalar controller at an initial speed of 50 rad/s. This method also presents two different transients and a steady-state operating region for the machine. The system is commanded to produce maximum torque at $t = 0.26$ s, and the machine entered the first transient region. The current transients are shown in Fig. 4.17(a). The augmentation method is turned off and conventional scalar control is activated at $t = 0.37$ s. Likewise with the DTC-based method, the system slows down to initial speed. The current transient can be seen in Fig. 4.18. Figure 4.19 shows the transition to steady-state operation. Different than DTC-based implementation, IFOC-based augmentation is subject to large current spikes between transitions. The current spike observed in this method is approximately 15 A with a 20 ms duration and can be seen in Fig. 4.20.

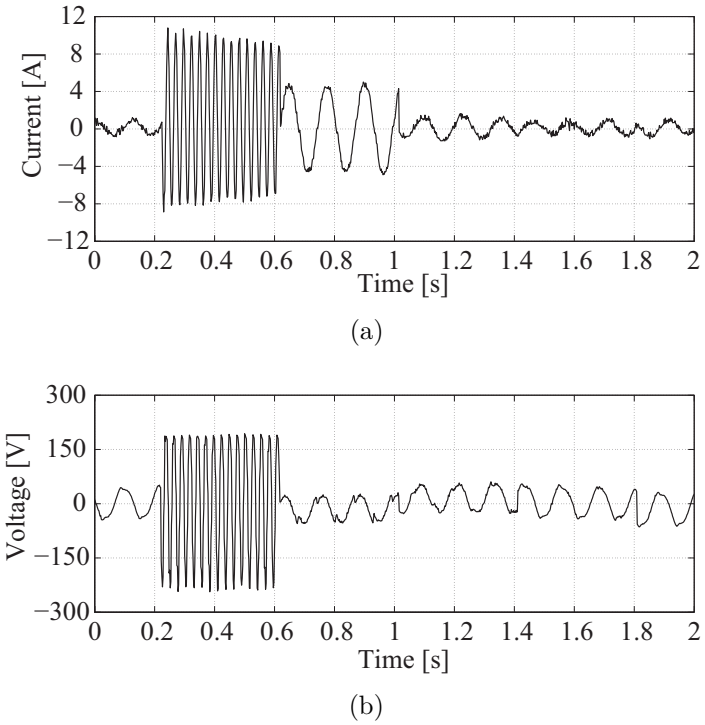

Figure 4.12: DTC-based augmentation method. (a) Phase A current and (b) phase A voltage.

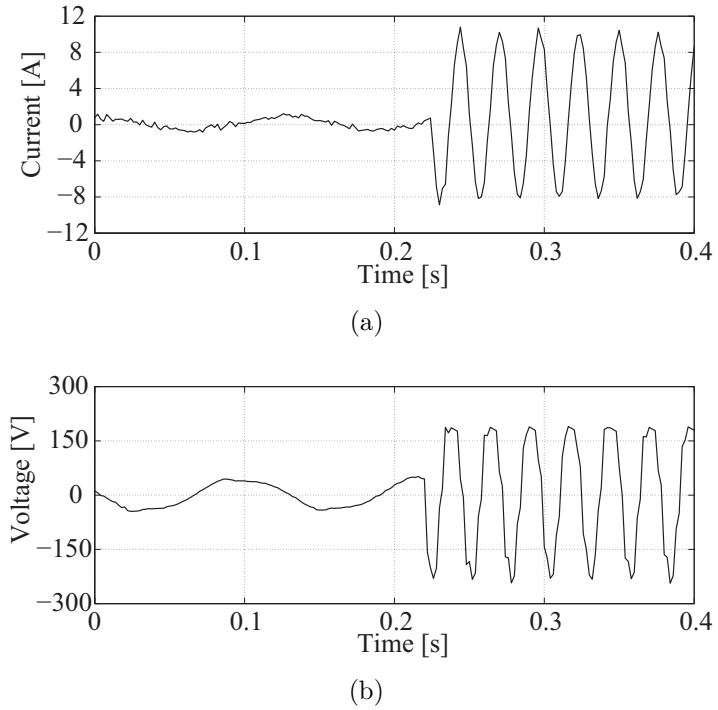

Figure 4.13: Switching from conventional scalar to DTC-based augmented controller. (a) Phase A current and (b) phase A voltage.

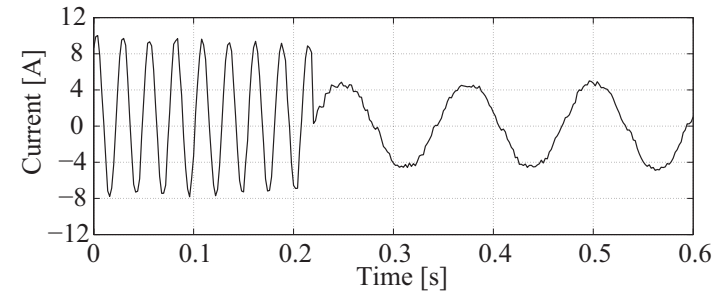

(a)

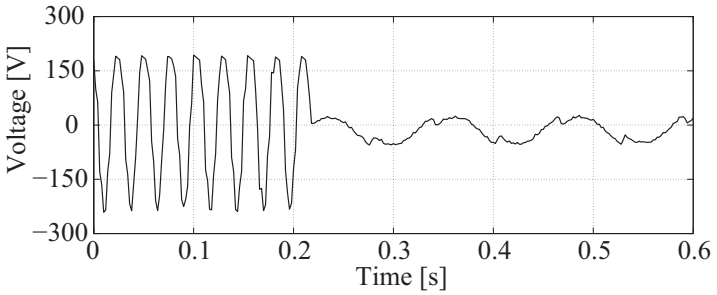

(b)

Figure 4.14: Switching from DTC-based augmented controller to conventional scalar controller. (a) Phase A current and (b) phase A voltage.

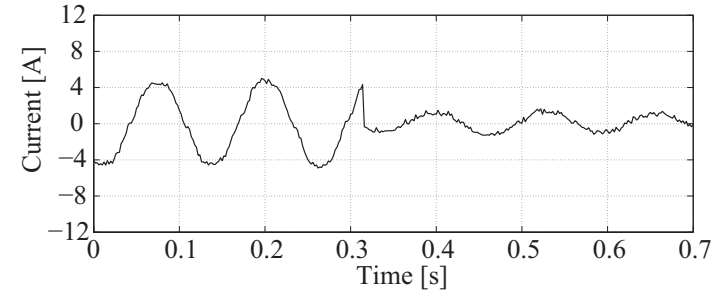

(a)

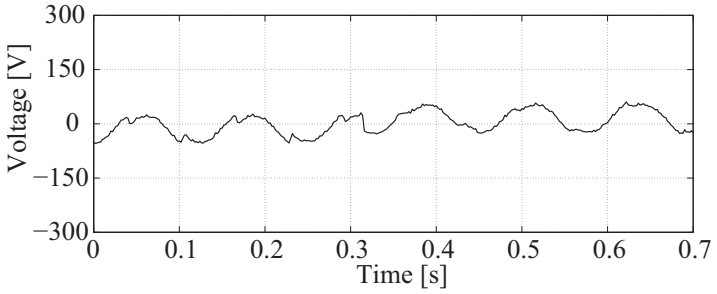

(b)

Figure 4.15: Scalar controller transition to steady-state. (a) Phase A current and (b) phase A voltage.

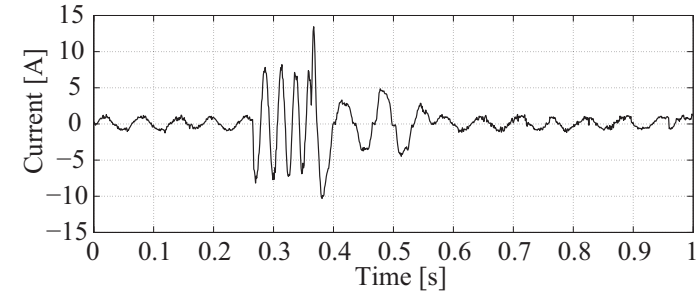

(a)

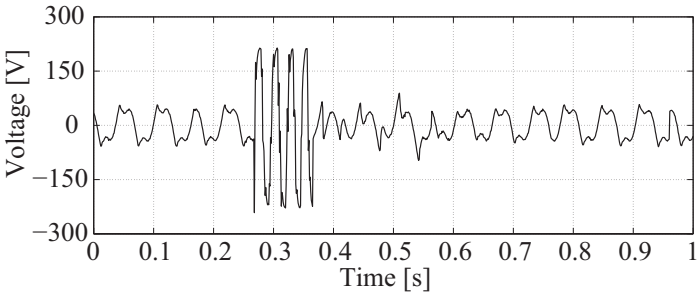

(b)

Figure 4.16: IFOC-based augmentation method. (a) Phase A current during transients and (b) phase A voltage.

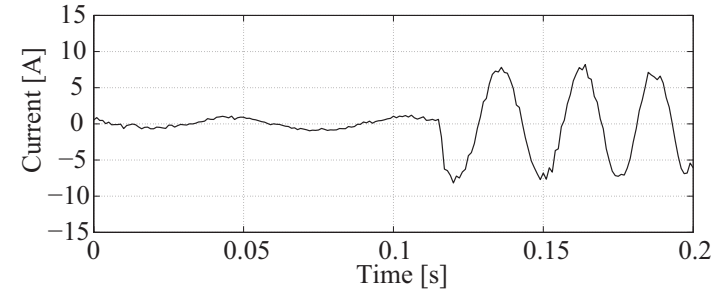

(a)

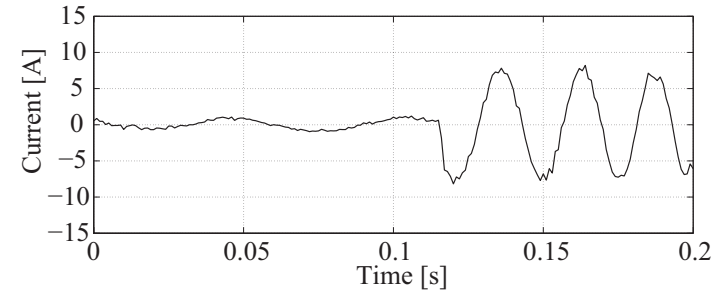

(b)

Figure 4.17: Switching from conventional scalar to IFOC-based augmented controller. (a) Phase A current and (b) phase A voltage.

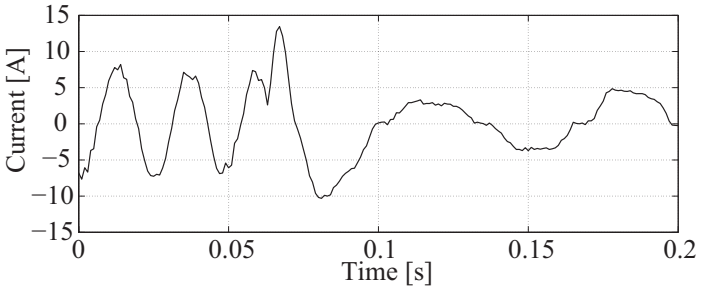

(a)

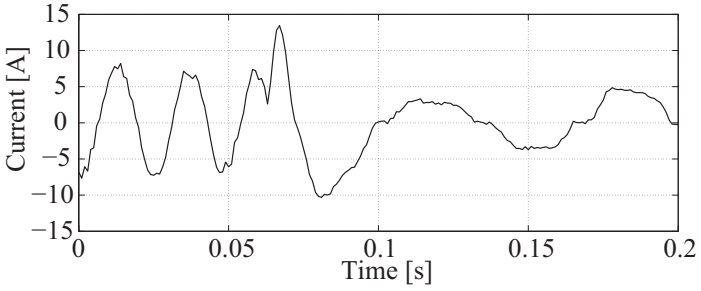

(b)

Figure 4.18: Switching from IFOC-based augmented controller to conventional scalar controller. (a) Phase A current and (b) phase A voltage.

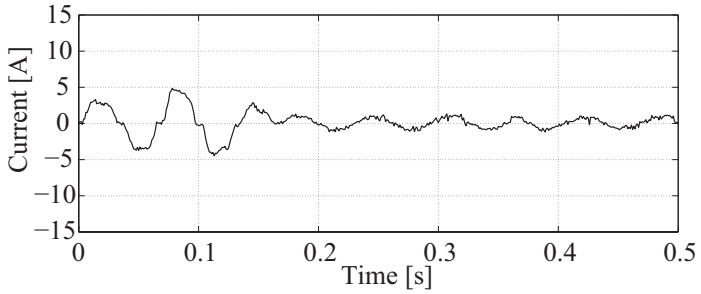

(a)

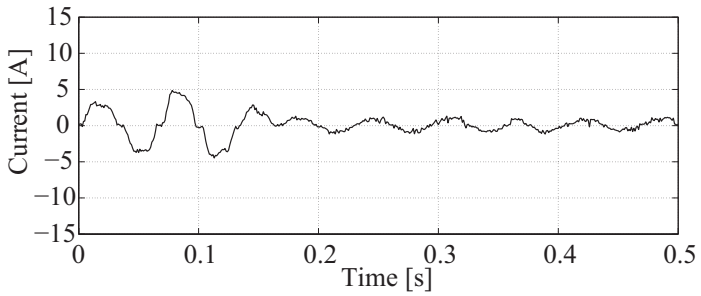

(b)

Figure 4.19: Scalar controller transition to steady state. (a) Phase A current and (b) phase A voltage.

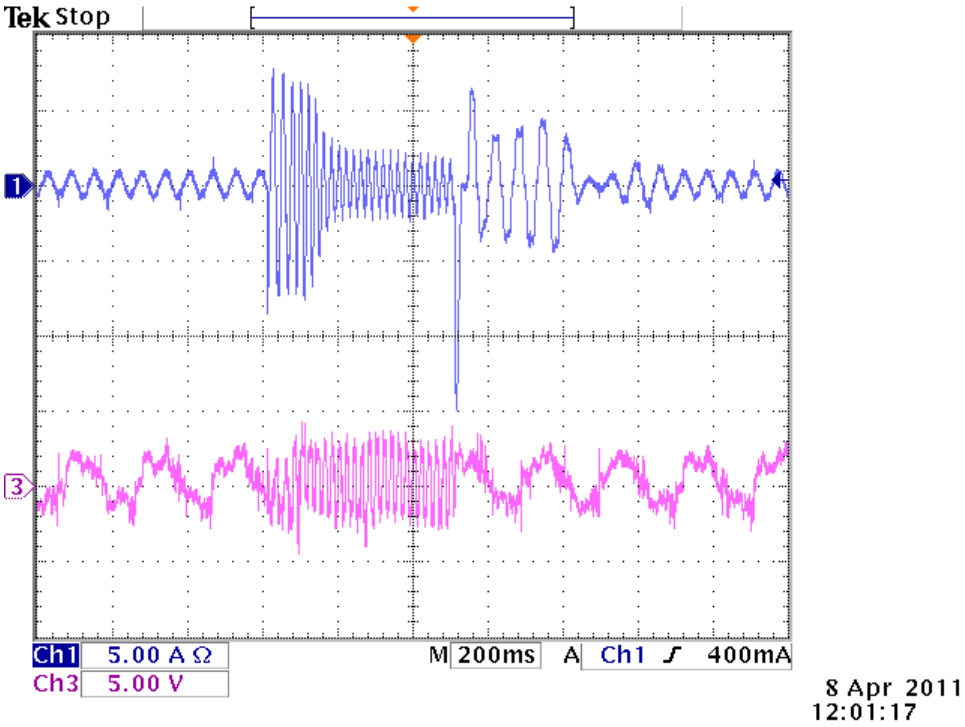

Figure 4.20: Transient response of the currents; top trace is the current and the bottom trace is the voltage (note the large current spike).

CHAPTER 5

CONCLUSION AND FUTURE WORK

This thesis focused on DTC implementation and performance improvement. Parameter sensitivities and instability issues associated with stator resistance were provided. The torque-speed coupling problem was experimentally evaluated and compensation methods were discussed. Maximum instantaneous torque capabilities of existing control methods were investigated. Comparative theoretical analyses of performance ranges for these methods were provided and experimentally justified. An augmentation algorithm to ensure decoupling using a look-up table was proposed.

Background information on induction machine modeling and an extensive literature review on derivations of controllers were provided. Field-oriented controllers and parameter sensitivities were discussed. According to the discussion, using stator field orientation provides faster torque response compared to rotor field orientation. However, the parameter sensitivity analysis showed that parameter mismatch problems can be avoided largely with the indirect field orientation method. A less parameter sensitive control method, DTC, was presented. The mathematical background of the work presented was based on the derivations and models presented in Chapter 2.

DTC implementation and performance issues were discussed. Extensive stator resistance sensitivity analysis was provided and the instability phenomenon with overestimated stator resistance was shown. The effect of increasing the resolution was illustrated. The results show that better angle resolution provides flexibility in torque and flux regulation, while minimum ripple can be achieved with a continuous flux angle approach.

Performance deterioration in a DTC drive due to coupling of electromagnetic torque, rotor speed, and stator flux, which results in reduced torque and speed capability and high torque ripple, was experimentally demonstrated. These problems were solved by two different techniques. Ideal IOD provides performance advantages, but requires real-time state values, and is

susceptible to noise. An AIOD method uses state reference values rather than the states themselves. Given sufficient inverter voltage capability, this method provides stable extended torque and speed capability. The cost is that feedback-based decoupling methods reduce voltage headroom to be used for torque and flux regulation, slowing the response.

Maximum instantaneous torque capabilities and methods to extract maximum possible torque from an induction machine were addressed. Voltage trade-offs associated with scalar control of induction machines motivate the study of methods capable of complete bus voltage utilization for high instantaneous torque. This trade-off can be avoided with vector controllers. Peak torque capabilities of two common vector controllers, FOC and DTC, were analyzed. Framed as a optimization problem, dc bus voltage and magnetic flux saturation become nonlinear performance constraints.

Stability investigation of continuous flux angle DTC showed that stable DTC operation is possible only if the controller gains (and bus voltages) are sufficiently high. These constraints limit torque generation capability, leading to a sub-optimal vector control approach for torque maximization. However, analytical solutions show that DTC provides higher peak torque capabilities, compared to FOC, at low speeds.

An augmentation algorithm for scalar controllers, which can be derived using DTC-based or IFOC-based approximations, was proposed. It is shown that the DTC-based approach produces higher torque compared to the IFOC-based approach in the low speed range. The DTC-based augmented scalar method provides fast torque response with a peak torque capability comparable to DTC and FOC and uses a simpler approach that can be implemented on a vectorized V/f controller. With this method, DTC- and FOC-based approaches can be combined to maximize momentary torque over the entire speed range.

Throughout this thesis, several future research topics have been identified. Induction machine limitations should be investigated regardless of the control method employed in order to implement methods that are capable of extracting the physical capabilities. In addition, time and thermal limitations should be included in the maximum machine capability investigations to provide further insight on operating durations. Furthermore, physical limitations of control methods and the machines should be experimentally justified.

A hybrid augmented scalar controller is viable and should be investigated as future research. Given the results on maximum instantaneous capabilities, the operating speed range of an induction machine can be divided into regions, and a time-optimal maximum torque controller consisting of FOC-and DTC-based approaches can be employed for optimal torque in the operating speed range. The commercialization of these high-current high-momentary torque augmentation methods is expected to enhance several applications including traction and electromagnetic launch.

APPENDIX A

SCALAR CONTROL WITH RESISTIVE COMPENSATION

A.1 Induction Machine Model

The induction machine model in the synchronous reference frame is represented as follows:

$$\mathbf{d\lambda_{qs}} = -r_s \mathbf{i_{qs}} - \omega_s \boldsymbol{\lambda}_{\mathbf{ds}} + \mathbf{v_{qs}};$$
$$\mathbf{d\lambda_{ds}} = -r_s \mathbf{i_{ds}} + \omega_s \boldsymbol{\lambda}_{\mathbf{qs}} + \mathbf{v_{ds}};$$
$$\mathbf{d\lambda_{qr}} = -r_r \mathbf{i_{qr}} - (\omega_s - n_p\omega)\, \boldsymbol{\lambda}_{\mathbf{dr}} + \mathbf{v_{qr}};$$
$$\mathbf{d\lambda_{dr}} = -r_r \mathbf{i_{dr}} + (\omega_s - n_p\omega)\, \boldsymbol{\lambda}_{\mathbf{qr}} + \mathbf{v_{dr}};$$

The algebraic relationships of rotor and stator fluxes are given below:

$$\boldsymbol{\lambda}_{\mathbf{qs}} = L_s \mathbf{i_{qs}} + L_m \mathbf{i_{qr}};$$
$$\boldsymbol{\lambda}_{\mathbf{ds}} = L_s \mathbf{i_{ds}} + L_m \mathbf{i_{dr}};$$
$$\boldsymbol{\lambda}_{\mathbf{qr}} = L_r \mathbf{i_{qr}} + L_m \mathbf{i_{qs}};$$
$$\boldsymbol{\lambda}_{\mathbf{dr}} = L_r \mathbf{i_{dr}} + L_m \mathbf{i_{ds}};$$

The implementation on a squirrel cage induction machine with resistive compensation can be defined as

$$\boldsymbol{v}_{\mathbf{qs}} = \boldsymbol{v}_{\mathbf{Qs}} + \boldsymbol{i}_{\mathbf{qs}} \boldsymbol{r}_{\boldsymbol{s}};$$
$$\boldsymbol{v}_{\mathbf{ds}} = \boldsymbol{v}_{\mathbf{Ds}} + \boldsymbol{i}_{\mathbf{ds}} \boldsymbol{r}_{\boldsymbol{s}};$$
$$\boldsymbol{v}_{\mathbf{qr}} = 0;$$
$$\boldsymbol{v}_{\mathbf{dr}} = 0;$$

A.2 Solution to Machine Model

In the synchronous frame, the steady-state solution to the machine can be found using

$$i_{\mathrm{dq}} = \mathrm{Solve}\left[\left\{\mathrm{d}\lambda_{\mathrm{qs}} == 0, \mathrm{d}\lambda_{\mathrm{qr}} == 0, \mathrm{d}\lambda_{\mathrm{ds}} == 0, \mathrm{d}\lambda_{\mathrm{dr}} == 0\right\}, \left\{i_{\mathrm{qs}}, i_{\mathrm{qr}}, i_{\mathrm{ds}}, i_{\mathrm{dr}}\right\}\right][[1]];$$
$$i_{\mathrm{qsss}} = \mathrm{FullSimplify}\left[i_{\mathrm{qs}}/.i_{\mathrm{dq}}\right];$$
$$i_{\mathrm{qrss}} = \mathrm{FullSimplify}\left[i_{\mathrm{qr}}/.i_{\mathrm{dq}}\right];$$
$$i_{\mathrm{dsss}} = \mathrm{FullSimplify}\left[i_{\mathrm{ds}}/.i_{\mathrm{dq}}\right];$$
$$i_{\mathrm{drss}} = \mathrm{FullSimplify}\left[i_{\mathrm{dr}}/.i_{\mathrm{dq}}\right];$$
$$T = \frac{3}{2} n_p \frac{L_m}{L_r}\left(i_{\mathrm{qs}}\lambda_{\mathrm{dr}} - i_{\mathrm{ds}}\lambda_{\mathrm{qr}}\right)/.\left\{i_{\mathrm{qs}} \to i_{\mathrm{qsss}}, i_{\mathrm{qr}} \to i_{\mathrm{qrss}}, i_{\mathrm{ds}} \to i_{\mathrm{dsss}}, i_{\mathrm{dr}} \to i_{\mathrm{drss}}\right\};$$

The parameters of the sample machine model are

$$v_{\mathrm{Qs}} = V;$$
$$v_{\mathrm{Ds}} = 0;$$
$$r_s = 0.6837;$$
$$L_{\mathrm{ls}} = 0.004152;$$
$$r_r = 0.451;$$
$$L_{\mathrm{lr}} = 0.004152;$$
$$L_m = 0.1486;$$
$$n_p = 2;$$
$$L_r = L_m + L_{\mathrm{lr}};$$
$$L_s = L_m + L_{\mathrm{ls}};$$

The torque-speed curve of the machine is obtained by

$$\mathrm{Plot}\left[\mathrm{Evaluate}\left[\mathrm{Table}\left[T/.\left\{V \to \mathrm{Piecewise}[\{\{j, j \le 377\}, \{377, j > 377\}\}], \omega_s \to j\right\},\right.\right.\right.$$
$$\left.\left.\left.\{j, 240, 241, 10\}\right]\right], \{\omega, -187, 377\}, \mathrm{PlotRange} \to \{\{-100, 377\}, \{-180, 180\}\},$$
$$\mathrm{AxesLabel} \to \{"\omega_r \text{ [rad/s]}", "T_e \text{ [N.m]}"\}]$$

and is given in Fig. A.1.

The breakdown torque of the induction machine is found by

$$\mathrm{MaxT} = \mathrm{Table}[\mathrm{Maximize}[T/.\{V \to \mathrm{Piecewise}[\{\{2 * \pi * j, j \le 60\}, \{375, j > 60\}\}],$$

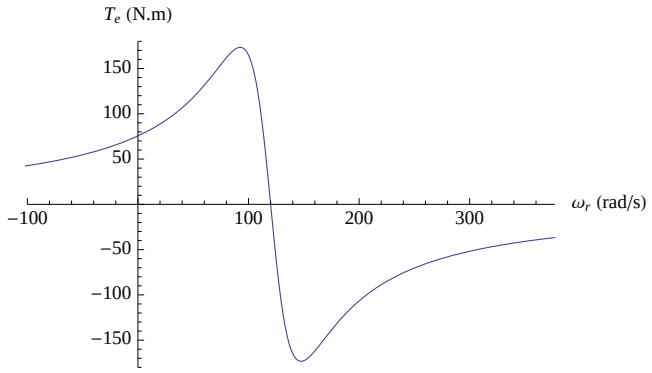

Figure A.1: Induction machine torque vs. speed curve under constant frequency excitation.

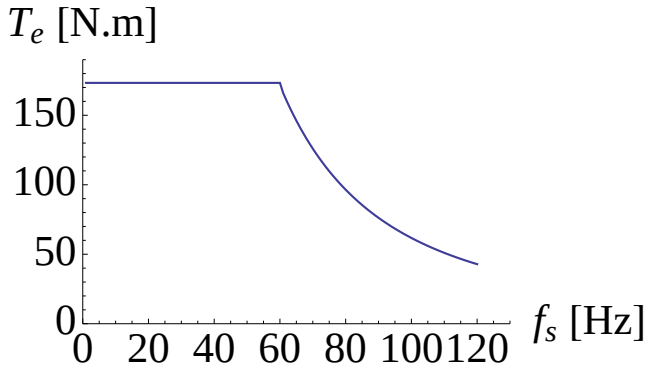

Figure A.2: Induction machine torque vs. stator frequency peak torque characteristic curve.

```
ωs → 2 * π * j} , ω] , {j, 1, 120, 1}] ;
L1 = Table[MaxT[[i, 1]], {i, 1, 120}];
L2 = Table[j, {j, 1, 120, 1}];
LL = {L2, L1};
ListLinePlot[{Transpose[LL]}, PlotRange → {{0, 130}, {0, 190}},
AxesLabel → {"fs [Hz]", "Te [N.m]"} , BaseStyle → {20, FontFamily → "Times"},
PlotStyle → {Thickness[0.005], Thickness[0.005]},
PlotMarkers → {{""}, {""}, {"|"}}]
```

and is given in Fig. A.2.

APPENDIX B

FIELD ORIENTED CONTROL MAXIMUM TORQUE CAPABILITIES

B.1 Induction Machine Model

The induction machine model in the rotor reference frame is represented as follows:

$$\mathbf{d\lambda_{qr}} = \frac{-r_r}{L_r}\lambda_{\mathbf{qr}} - \left(\frac{r_r}{L_r}L_m\frac{(i_{\mathbf{qs}}\lambda_{\mathbf{dr}} - i_{\mathbf{ds}}\lambda_{\mathbf{qr}})}{\lambda_{\mathbf{dr}}\text{^}2+\lambda_{\mathbf{qr}}\text{^}2}\right)\lambda_{\mathbf{dr}} + \frac{r_r}{L_r}L_m i_{\mathbf{qs}};$$
$$\mathbf{d\lambda_{dr}} = \frac{-r_r}{L_r}\lambda_{\mathbf{dr}} + \left(\frac{r_r}{L_r}L_m\frac{(i_{\mathbf{qs}}\lambda_{\mathbf{dr}} - i_{\mathbf{ds}}\lambda_{\mathbf{qr}})}{\lambda_{\mathbf{dr}}\text{^}2+\lambda_{\mathbf{qr}}\text{^}2}\right)\lambda_{\mathbf{qr}} + \frac{r_r}{L_r}L_m i_{\mathbf{ds}};$$
$$\mathbf{di_{ds}} = \frac{L_m r_r}{\sigma {L_r}^2}\lambda_{\mathbf{dr}} + \frac{n_p\omega L_m}{\sigma L_r}\lambda_{\mathbf{qr}} + \omega_e i_{\mathbf{qs}} - \gamma i_{\mathbf{ds}} + \frac{1}{\sigma}v_{\mathbf{ds}};$$
$$\mathbf{di_{qs}} = \frac{-n_p\omega L_m}{\sigma L_r}\lambda_{\mathbf{dr}} + \frac{L_m r_r}{\sigma {L_r}^2}\lambda_{\mathbf{qr}} - \omega_e i_{\mathbf{ds}} - \gamma i_{\mathbf{qs}} + \frac{1}{\sigma}v_{\mathbf{qs}};$$

First derivative of torque and the slip definition:

$$\mathbf{d\tau} = \mathbf{d\lambda_{dr}}i_{\mathbf{qs}} + \lambda_{\mathbf{dr}}\mathbf{di_{qs}} - \mathbf{d\lambda_{qr}}i_{\mathbf{ds}} - \lambda_{\mathbf{qr}}\mathbf{di_{ds}};$$
$$\omega_e = n_p\omega + \frac{r_r}{L_r}L_m\frac{(i_{\mathbf{qs}}\lambda_{\mathbf{dr}} - i_{\mathbf{ds}}\lambda_{\mathbf{qr}})}{\lambda_{\mathbf{dr}}\text{^}2+\lambda_{\mathbf{qr}}\text{^}2};$$

The implementation on a squirrel cage induction machine with FOC input voltages:

$$v_{\mathbf{ds}} = \sigma\left(-n_p\omega i_{\mathbf{qs}} - \frac{r_r}{L_r}L_m i_{\mathbf{qs}}\frac{(i_{\mathbf{qs}}\lambda_{\mathbf{dr}} - i_{\mathbf{ds}}\lambda_{\mathbf{qr}})}{\lambda_{\mathbf{dr}}\text{^}2+\lambda_{\mathbf{qr}}\text{^}2} - u_{\mathbf{speed}}\frac{\lambda_{\mathbf{qr}}}{\sqrt{\lambda_{\mathbf{dr}}\text{^}2+\lambda_{\mathbf{qr}}\text{^}2}} + u_{\mathbf{flux}}\frac{\lambda_{\mathbf{dr}}}{\sqrt{\lambda_{\mathbf{dr}}\text{^}2+\lambda_{\mathbf{qr}}\text{^}2}}\right) - \frac{L_m}{L_r}n_p\omega\lambda_{\mathbf{qr}};$$
$$v_{\mathbf{qs}} = \sigma\left(n_p\omega i_{\mathbf{ds}} + \frac{r_r}{L_r}L_m i_{\mathbf{ds}}\frac{(i_{\mathbf{qs}}\lambda_{\mathbf{dr}} - i_{\mathbf{ds}}\lambda_{\mathbf{qr}})}{\lambda_{\mathbf{dr}}\text{^}2+\lambda_{\mathbf{qr}}\text{^}2} + u_{\mathbf{speed}}\frac{\lambda_{\mathbf{dr}}}{\sqrt{\lambda_{\mathbf{dr}}\text{^}2+\lambda_{\mathbf{qr}}\text{^}2}} + u_{\mathbf{flux}}\frac{\lambda_{\mathbf{qr}}}{\sqrt{\lambda_{\mathbf{dr}}\text{^}2+\lambda_{\mathbf{qr}}\text{^}2}}\right) + \frac{L_m}{L_r}n_p\omega\lambda_{\mathbf{dr}};$$

B.2 Solution to Machine Model under FOC

In the rotor frame, the steady-state solution to the machine can be found using

$$\text{varplsb2} = \text{Solve}\left[\{\text{di}_{\text{qs}} == 0, \text{di}_{\text{ds}} == 0, \text{d}\lambda_{\text{qr}} == 0, \text{d}\lambda_{\text{dr}} == 0\},\right.$$
$$\left.\{i_{\text{qs}}, i_{\text{ds}}, \lambda_{\text{qr}}, \lambda_{\text{dr}}\}\right][[5]];$$
$$i_q = i_{\text{qs}}/.\text{varplsb2};$$
$$i_d = i_{\text{ds}}/.\text{varplsb2};$$
$$\lambda_q = \lambda_{\text{qr}}/.\text{varplsb2};$$
$$\lambda_d = \lambda_{\text{dr}}/.\text{varplsb2};$$
$$\tau = i_q\lambda_d - i_d\lambda_q//\text{FullSimplify};$$

The parameters of the sample machine model are

$$r_s = 0.6837;$$
$$L_{\text{ls}} = 0.004152;$$
$$r_r = 0.451;$$
$$L_{\text{lr}} = 0.004152;$$
$$L_m = 0.1486;$$
$$L_s = L_m + L_{\text{ls}};$$
$$L_r = L_m + L_{\text{lr}};$$
$$\sigma = \frac{L_s L_r - L_m\text{\^{}}2}{L_r};$$
$$\gamma = \frac{L_m{}^2 r_r + L_r{}^2 r_s}{\sigma L_r{}^2};$$
$$n_p = 2;$$

The input voltages and constraints are defined as

$$v_{\text{ds}} = v_{\text{ds}}/.\{i_{\text{qs}} \to i_q, i_{\text{ds}} \to i_d, \lambda_{\text{dr}} \to \lambda_d, \lambda_{\text{qr}} \to \lambda_q\};$$
$$v_{\text{qs}} = v_{\text{qs}}/.\{i_{\text{qs}} \to i_q, i_{\text{ds}} \to i_d, \lambda_{\text{dr}} \to \lambda_d, \lambda_{\text{qr}} \to \lambda_q\};$$
$$\text{V1} = v_{\text{ds}}\text{\^{}}2 + v_{\text{qs}}\text{\^{}}2;$$

The solution for u_{speed} can be found as

$$\text{var214} = u_{\text{speed}}/.\text{Solve}\left[\text{V1} == 460 * 460 * 2/3, u_{\text{speed}}\right][[4]];$$
$$V = \sqrt{\text{V1}}/.u_{\text{speed}} \to \text{var214};$$

$$T = \tau /. u_{\text{speed}} \rightarrow \text{var214};$$

The optimal u_{flux} can be found by solving the torque relationship as

$$\omega_{\text{init}} = 10;$$
$$\omega_{\text{end}} = 90;$$
$$\omega_{\text{step}} = 10;$$
$$\text{Tmax1} = \text{Table}\left[\text{NMaximize}\left[\{\text{Re}[T], u_{\text{flux}} < -650\}, u_{\text{flux}}, \right.\right.$$
$$\left.\left.\text{MaxIterations} \rightarrow 300\right], \{\omega, \omega_{\text{init}}, \omega_{\text{end}}, \omega_{\text{step}}\}\right];$$
$$\omega_{\text{init}} = 100;$$
$$\omega_{\text{end}} = 190;$$
$$\omega_{\text{step}} = 10;$$
$$\text{Tmax2} = \text{Table}\left[\text{NMaximize}\left[\{\text{Re}[T], -800 < u_{\text{flux}} < -250\}, u_{\text{flux}}, \right.\right.$$
$$\left.\left.\text{MaxIterations} \rightarrow 300\right], \{\omega, \omega_{\text{init}}, \omega_{\text{end}}, \omega_{\text{step}}\}\right];$$
$$\omega_{\text{init}} = 200;$$
$$\omega_{\text{end}} = 290;$$
$$\omega_{\text{step}} = 10;$$
$$\text{Tmax3} = \text{Table}\left[\text{NMaximize}\left[\{\text{Re}[T], -450 < u_{\text{flux}} < -150\}, u_{\text{flux}}, \right.\right.$$
$$\left.\left.\text{MaxIterations} \rightarrow 300\right], \{\omega, \omega_{\text{init}}, \omega_{\text{end}}, \omega_{\text{step}}\}\right];$$
$$\omega_{\text{init}} = 300;$$
$$\omega_{\text{end}} = 380;$$
$$\omega_{\text{step}} = 10;$$
$$\text{Tmax4} = \text{Table}\left[\text{NMaximize}\left[\{\text{Re}[T], -300 < u_{\text{flux}} < -55\}, u_{\text{flux}}, \right.\right.$$
$$\left.\left.\text{MaxIterations} \rightarrow 300\right], \{\omega, \omega_{\text{init}}, \omega_{\text{end}}, \omega_{\text{step}}\}\right];$$

The torque solution is found by dividing the solution space into four parts. This solution method is utilized because the bounds on possible solution space is very large. This way, faster simulations and more accurate results are obtained. The maximum theoretical torque vs. speed curve is given in Fig. B.1.

$$\text{L1} = \text{Table}[\text{Tmax1}[[i, 1]], \{i, 1, \text{Dimensions}[\text{Tmax1}][[1]]\}];$$
$$\text{L2} = \text{Table}[\text{Tmax2}[[i, 1]], \{i, 1, \text{Dimensions}[\text{Tmax2}][[1]]\}];$$
$$\text{L111} = \text{Table}[\text{Tmax3}[[i, 1]], \{i, 1, \text{Dimensions}[\text{Tmax3}][[1]]\}];$$
$$\text{L121} = \text{Table}[\text{Tmax4}[[i, 1]], \{i, 1, \text{Dimensions}[\text{Tmax4}][[1]]\}];$$
$$\text{L3} = u_{\text{flux}} /. \text{Table}[\text{Tmax1}[[i, 2]], \{i, 1, \text{Dimensions}[\text{Tmax1}][[1]]\}];$$

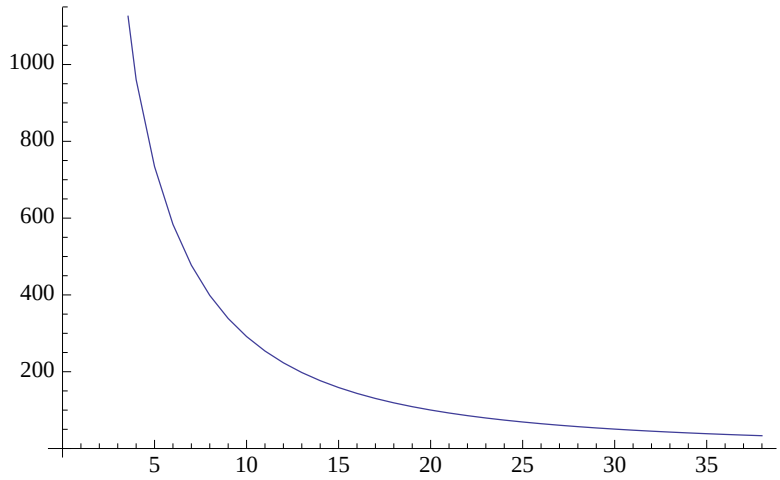

Figure B.1: Induction machine torque vs. stator frequency peak torque characteristic curve under FOC.

```
L4 = u_flux/.Table[Tmax2[[i, 2]], {i, 1, Dimensions[Tmax2][[1]]}];
L13 = u_flux/.Table[Tmax3[[i, 2]], {i, 1, Dimensions[Tmax3][[1]]}];
L14 = u_flux/.Table[Tmax4[[i, 2]], {i, 1, Dimensions[Tmax4][[1]]}];
L5 = 3/2 n_p L_m/L_r * Join[L1, L2, L111, L121];
L0 = Table[ω, {ω, 10, 190, 10}];
L6 = Table[ω, {ω, 200, 380, 10}];
L8 = Join[L0, L6];
L9 = {L8, L5};
ListLinePlot[L5]
```

This solution corresponds to the optimal torque from the machine without constrained rotor flux.

```
V2 = Sqrt[v_ds^2 + v_qs^2];
var22 = u_speed/.Solve[V2 == 375.58, {u_speed}][[4]];
τ1 = (i_q λ_d − i_d λ_q)/.u_speed → var22;
T2 = {Table[j, {j, 1, 380, 10}], Table[3/2 n_p L_m/L_r τ1/.{u_flux → −393.188, ω → j},
{j, 1, 380, 10}]};
ListLinePlot[{Transpose[T2], Transpose[L9]}]
```

The speed at which the torque curves in Fig. B.2 are tangential corresponds to the critical rotor speed. At this point, the optimal torque approach is

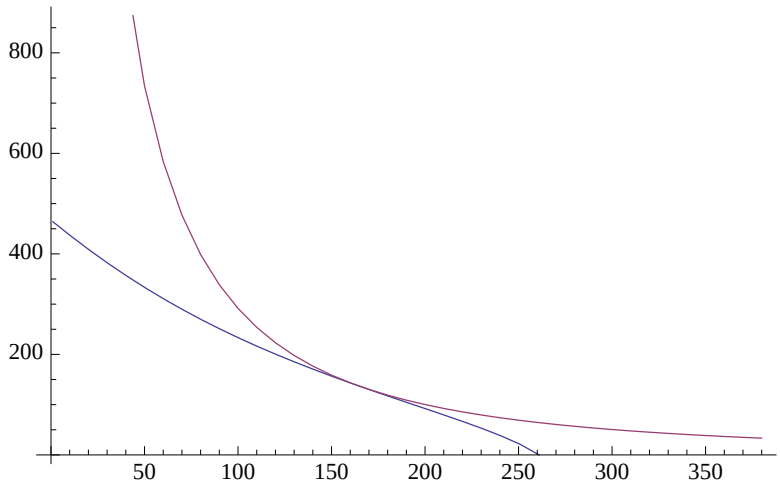

Figure B.2: Comparative induction machine torque vs. speed curve under FOC with optimal (neglecting saturation) and rated rotor fluxes.

required to start flux reduction. The output maximum torque comparison can be seen by computing the torque with different rotor flux commands. The comparison is given in Fig. B.3.

$$\mathbf{T3 = \left\{Table[j, \{j, 1, 380, 10\}], Table\left[\frac{3}{2} n_p \frac{L_m}{L_r} \tau 1 /. \{u_{flux} \to -337.018, \omega \to j\}\right], \{j, 1, 380, 10\}]\right\};}$$

$$\mathbf{T4 = \left\{Table[j, \{j, 1, 380, 10\}], Table\left[\frac{3}{2} n_p \frac{L_m}{L_r} \tau 1 /. \{u_{flux} \to -280.849, \omega \to j\}\right], \{j, 1, 380, 10\}]\right\};}$$

$$\mathbf{T5 = \left\{Table[j, \{j, 1, 380, 10\}], Table\left[\frac{3}{2} n_p \frac{L_m}{L_r} \tau 1 /. \{u_{flux} \to -224.679, \omega \to j\}\right], \{j, 1, 380, 10\}]\right\};}$$

$$\mathbf{ListLinePlot[\{Transpose[T2], Transpose[T3], Transpose[T4], Transpose[T5]\}]}$$

In reality, saturation cannot be neglected. The optimal torque output of the machine under constrained voltage and rotor flux is found using

$$\mathbf{K1 = Table[Min[Re[T2[[2, j + 1]]], Re[L9[[2, j]]]], \{j, 1, 16, 1\}];}$$

$$\mathbf{J1 = Table[Re[T2[[1, j + 1]]], \{j, 1, 16, 1\}];}$$

$$\mathbf{K2 = Table[Max[Re[T2[[2, j + 1]]], Re[L9[[2, j]]]], \{j, 17, 37, 1\}];}$$

$$\mathbf{J2 = Table[Re[L9[[1, j + 1]]], \{j, 16, 36, 1\}];}$$

$$\mathbf{K3 = Table[Re[T2[[2, j]]], \{j, 1, 1, 1\}];}$$

$$\mathbf{J3 = Table[Re[T2[[1, j]]], \{j, 1, 1, 1\}];}$$

$$\mathbf{J = Join[J3, J1, J2];}$$

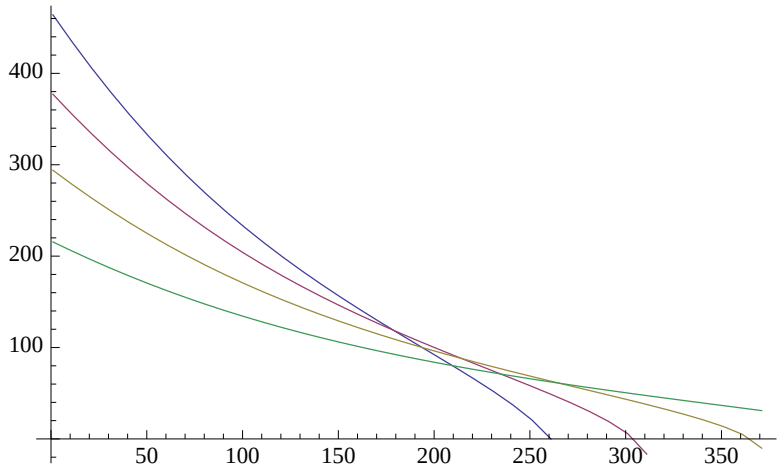

Figure B.3: Induction machine torque vs. speed curves under different rotor fluxes.

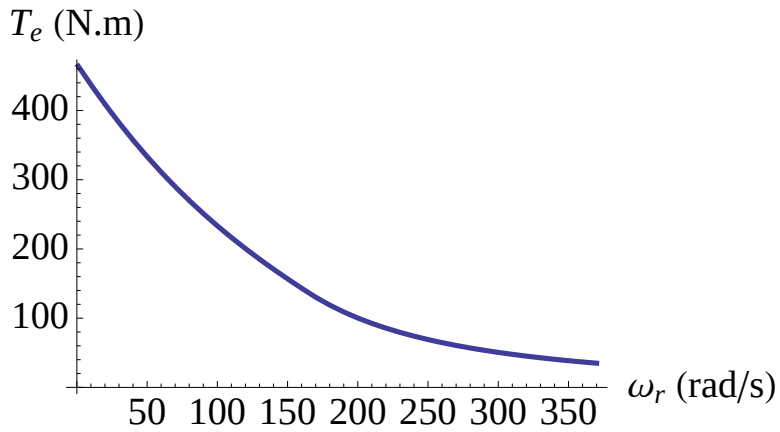

Figure B.4: Induction machine optimal practical torque vs. speed curve.

```
K = Join[K3, K1, K2];
Lcomb = {J, K};
Llim = Table[180, {j, 0, 10, 1}];
Lplot = Table[66 * j, {j, 0, 10, 1}];
Llimit = {Llim, Lplot};
ListLinePlot [{Transpose[Lcomb]}, AxesLabel → {"ωr (rad/s)", "Te (N.m)"},
BaseStyle → {15, FontFamily → "Times"}, PlotStyle → {AbsoluteThickness[2]},
PlotMarkers → {{""}, {"|"}}]
```

Figure B.4 provides the maximum possible torque at all speed ranges. The rotor flux below the critical speed is rated flux. This flux is reduced at higher speeds in order to obtain optimal torque above the critical speed.

APPENDIX C

DIRECT TORQUE CONTROL MAXIMUM TORQUE CAPABILITIES

C.1 Induction Machine Model

The induction machine model in the stationary reference frame is represented as follows:

$$\mathrm{d}\phi = -2\left(R_s\eta - \sqrt{\phi}u_F\right);$$
$$\mathrm{d}\rho = -R_s\frac{\tau}{\phi} + \frac{1}{\sqrt{\phi}}u_T;$$
$$\mathrm{d}\tau = \frac{1}{\sigma}\left(-\frac{\gamma}{L_s}\tau - \frac{n_p}{L_s}\omega\phi + \frac{1}{L_s}\sqrt{\phi}u_T\right) + n_p\omega\eta + \frac{1}{\sqrt{\phi}}\left(-\eta u_T + \tau u_F\right);$$
$$\mathrm{d}\eta = \frac{1}{\sigma}\left(-\frac{\gamma}{L_s}\eta - \frac{R_r}{L_sL_r}\phi + \frac{1}{L_s}\sqrt{\phi}u_F\right) - n_p\omega\tau - R_s\left(\frac{\eta\text{\^{}}2+\tau\text{\^{}}2}{\phi}\right) + \frac{1}{\sqrt{\phi}}\left(\eta u_F + \tau u_T\right);$$
$$\mathrm{d}\eta 2 = \frac{1}{\sigma}\left(-\frac{\gamma}{L_s}\eta - \frac{R_r}{L_sL_r}\phi + \frac{1}{L_s}\sqrt{\phi}u_F\right);$$

C.2 Solution to Machine Model under DTC

In the stationary frame, the steady-state solution to the machine can be found using:

```
var10 = Solve[{dτ == 0, dη == 0}, {τ, η}][[1]];
T1 = τ/.var10;
H1 = η/.var10;
var11 = η/.Solve[dη2 == 0, η][[1]];
df1 = dϕ/.{η → var11};
F1 = ϕ/.Solve[df1 == 0, ϕ][[2]];
```

The parameters of the sample machine model are:

```
Rs = 0.6837;
```

$L_{\text{ls}} = 0.004152;$
$R_r = 0.451;$
$L_{\text{lr}} = 0.004152;$
$L_m = 0.1486;$
$L_s = L_m + L_{\text{ls}};$
$L_r = L_m + L_{\text{lr}};$
$\sigma = \frac{L_s L_r - L_m \text{\^{}} 2}{L_r L_s};$
$\gamma = \frac{L_s R_r}{L_r} + R_s;$
$n_p = 2;$
$\text{T2} = \text{T1}/.\{\phi \to \text{F1}\};$

This approach elaborates on the sliding mode control approach as presented by Sorchini. The optimal u_F can be found by solving the torque relationship for constant torque as

$\omega_{\text{init}} = 5;$
$\omega_{\text{end}} = 95;$
$\omega_{\text{step}} = 5;$
$\text{Tmax1} = \text{Table}\left[\text{NMaximize}\left[\{\text{Re}[\text{T2}]/.u_T \to 125, -50 < u_F < 0\}, u_F,\right.\right.$
$\left.\left.\text{MaxIterations} \to 300\right], \{\omega, \omega_{\text{init}}, \omega_{\text{end}}, \omega_{\text{step}}\}\right];$
$\omega_{\text{init}} = 100;$
$\omega_{\text{end}} = 195;$
$\omega_{\text{step}} = 5;$
$\text{Tmax2} = \text{Table}\left[\text{NMaximize}\left[\{\text{Re}[\text{T2}]/.u_T \to 125, -5 < u_F < 0\}, u_F,\right.\right.$
$\left.\left.\text{MaxIterations} \to 300\right], \{\omega, \omega_{\text{init}}, \omega_{\text{end}}, \omega_{\text{step}}\}\right];$
$\omega_{\text{init}} = 200;$
$\omega_{\text{end}} = 295;$
$\omega_{\text{step}} = 5;$
$\text{Tmax3} = \text{Table}\left[\text{NMaximize}\left[\{\text{Re}[\text{T2}]/.u_T \to 125, -2 < u_F < 0\}, u_F,\right.\right.$
$\left.\left.\text{MaxIterations} \to 300\right], \{\omega, \omega_{\text{init}}, \omega_{\text{end}}, \omega_{\text{step}}\}\right];$
$\omega_{\text{init}} = 300;$
$\omega_{\text{end}} = 380;$
$\omega_{\text{step}} = 5;$
$\text{Tmax4} = \text{Table}\left[\text{NMaximize}\left[\{\text{Re}[\text{T2}]/.u_T \to 125, -1 < u_F < 0\}, u_F,\right.\right.$
$\left.\left.\text{MaxIterations} \to 300\right], \{\omega, \omega_{\text{init}}, \omega_{\text{end}}, \omega_{\text{step}}\}\right];$

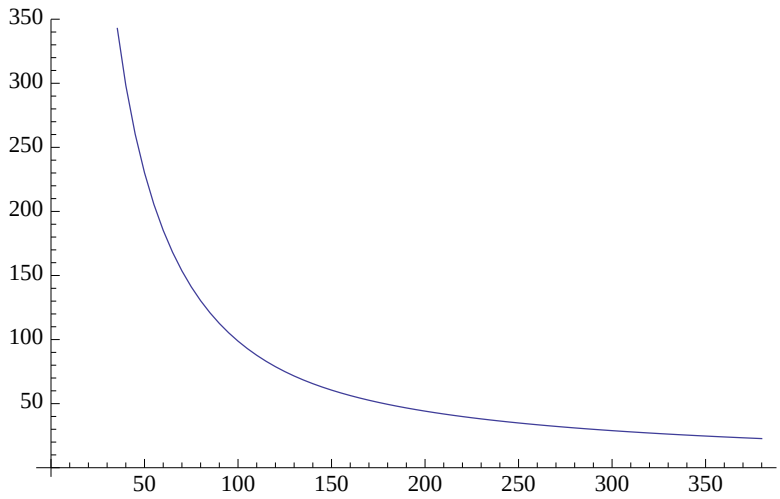

Figure C.1: Induction machine optimal theoretical torque vs. speed curve (neglecting saturation).

Given that the bounds on the possible solution space is very large, constraining the optimization at all operating speeds with the same bounds result in more iteration steps and slower convergence rate. Therefore optimal flux is found by dividing the solution space into four parts.

$$\mathbf{L1 = 3 * Table[Tmax1[[i, 1]], \{i, 1, Dimensions[Tmax1][[1]]\}];}$$
$$\mathbf{L2 = 3 * Table[Tmax2[[i, 1]], \{i, 1, Dimensions[Tmax2][[1]]\}];}$$
$$\mathbf{L3 = 3 * Table[Tmax3[[i, 1]], \{i, 1, Dimensions[Tmax3][[1]]\}];}$$
$$\mathbf{L4 = 3 * Table[Tmax4[[i, 1]], \{i, 1, Dimensions[Tmax4][[1]]\}];}$$
$$\mathbf{L5 = Join[L1, L2, L3, L4];}$$
$$\mathbf{L0 = Table[\omega, \{\omega, 5, 195, 5\}];}$$
$$\mathbf{L6 = Table[\omega, \{\omega, 200, 380, 5\}];}$$
$$\mathbf{L8 = Join[L0, L6];}$$
$$\mathbf{L9 = \{L8, L5\};}$$
$$\mathbf{ListLinePlot[Transpose[L9]]}$$

This solution corresponds to the optimal torque from the machine without constrained rotor flux. This is given in Fig. C.1.

$$\mathbf{Ta3 = Table\left[\{j, 3/2 * n_p * T2/. \{u_F \to -"1.79035", u_T \to 125, \omega \to j\}\}\right],}$$
$$\mathbf{\{j, 1, 380, 1\}];}$$
$$\mathbf{Ta4 = Table\left[\{j, 3/2 * n_p * T2/. \{u_F \to -"2.23794", u_T \to 125, \omega \to j\}\}\right],}$$

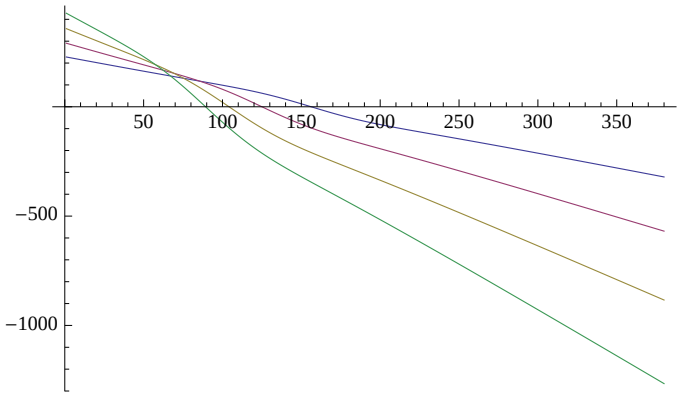

Figure C.2: Induction machine torque vs. speed curve under different rotor fluxes.

```
{j, 1, 380, 1}];
Ta5 = Table [{j, 3/2 * n_p * T2/. {u_F → −"2.68553", u_T → 125, ω → j}} ,
{j, 1, 380, 1}];
Ta6 = Table [{j, 3/2 * n_p * T2/. {u_F → −"3.13312", u_T → 125, ω → j}} ,
{j, 1, 380, 1}];
ListLinePlot[{Ta3, Ta4, Ta5, Ta6}]
```

Output maximum torque comparison can be seen by computing the torque with different rotor flux commands. The family of curves is given in Fig. C.2

```
K1 = Table[Min[Ta6[[5 * j, 2]], Re[L9[[2, j]]]], {j, 1, 10, 1}];
J1 = Table[Ta6[[5 * j, 1]], {j, 1, 10, 1}];
K2 = Table[Max[Ta6[[5 * j, 2]], Re[L9[[2, j]]]], {j, 11, 76, 1}];
J2 = Table[L9[[1, j]], {j, 11, 76, 1}];
K3 = Table[Ta6[[j, 2]], {j, 1, 4, 1}];
J3 = Table[Ta6[[j, 1]], {j, 1, 4, 1}];
K = Join[K3, K1, K2];
J = Join[J3, J1, J2];
Kcomb = {J, K};
ListLinePlot[{Transpose[L9], Ta6, Transpose[Kcomb]}]
```

Figure C.3 shows comparison of induction machine maximum electromagnetic torque under constant flux. The rotor speed where these torque curves are tangential to each other corresponds to the critical rotor speed where

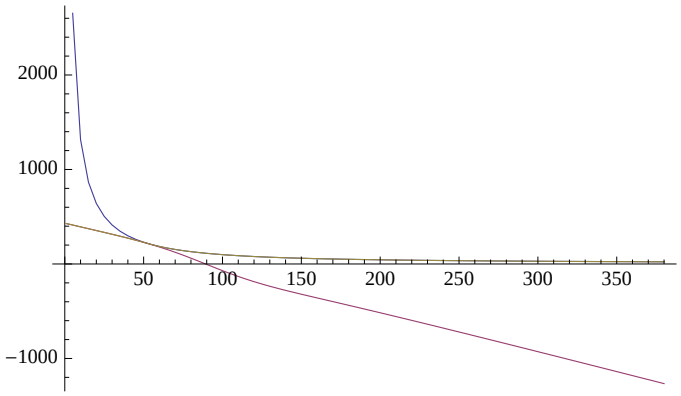

Figure C.3: Comparative induction machine torque vs. speed curve under DTC with optimal rotor flux (neglecting saturation) and constant rotor flux.

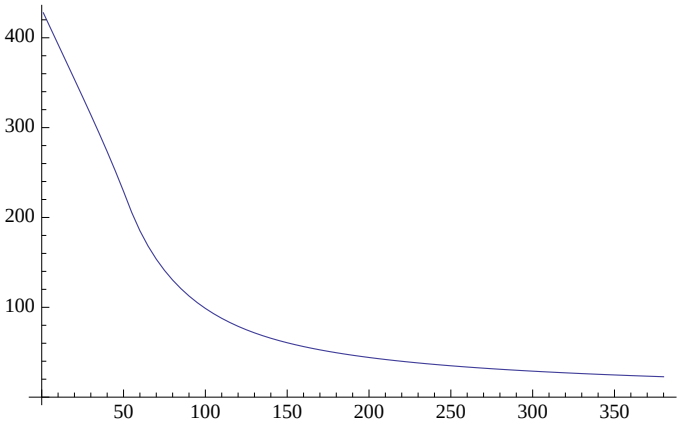

Figure C.4: Induction machine optimal practical torque vs. speed curve under DTC.

the optimal torque approach is required to start flux reduction. The optimal torque output of the machine under constrained voltage and rotor flux is found using

ListLinePlot[Transpose[Kcomb]]

Figure C.4 provides the maximum possible torque at all speed ranges. The rotor flux below the critical speed is rated flux. This flux is reduced at higher speeds in order to obtain optimal torque above the critical speed.

REFERENCES

[1] P. C. Krause, O. Wasynczuk, and S. D. Sudhoff, *Analysis of Electric Machinery and Drive Systems*, 2nd ed. Piscataway, NJ: IEEE Press, 2002.

[2] F. Blaschke, "The principle of field orientation as applied to the new transvektor closed-loop control system for rotating-field machines," *Siemens Rev.*, vol. 39, pp. 217 –220, 1972.

[3] I. Takahashi and T. Noguchi, "A new quick-response and high-efficiency control strategy of an induction motor," *IEEE Trans. Ind. Appl.*, vol. IA-22, no. 5, pp. 820 –827, 1986.

[4] M. Depenbrock, "Direct self-control (DSC) of inverter-fed induction machine," *IEEE Trans. Power Electron.*, vol. 3, no. 4, pp. 420 –429, Oct. 1988.

[5] Z. Sorchini, "A framework for the analysis and design of vector controllers for induction machines," Ph.D. dissertation, University of Illinois at Urbana-Champaign, Urbana, IL, Aug. 2006, tech. rep. CEME-TR-2006-08.

[6] Z. Sorchini and P. Krein, "Formal derivation of direct torque control for induction machines," *IEEE Trans. Power Electron.*, vol. 21, no. 5, pp. 1428 –1436, 2006.

[7] P. Vas, *Sensorless Vector and Direct Torque Control*. New York, NY: Oxford University Press, 1998.

[8] F. Disilvestro, "Comparative analysis and simulation of scalar and vector control methods for induction motors," M.S. thesis, University of Illinois at Urbana-Champaign, Urbana, IL, 1993.

[9] R. H. Park, "Two-reaction theory of synchronous machines - generalized method of analysis, part I," *AIEE Transactions*, vol. 48, pp. 716 –727, July 1929.

[10] D. S. Brereton, D. G. Lewis, and C. G. Young, "Representation of induction motor loads during power system stability studies," *AIEE Transactions*, vol. 76, pp. 451 –461, Aug. 1957.

[11] P. C. Krause and C. H. Thomas, "Simulation of symmetrical induction machinery," *IEEE Trans. Power Apparatus and Systems*, vol. 84, pp. 1038 –1053, Nov. 1965.

[12] A. M. Bazzi, "Designing better induction motor drive systems from efficiency, reliability, and power electronics perspectives," Ph.D. dissertation, University of Illinois at Urbana-Champaign, Urbana, IL, Nov. 2010, tech. rep. CEME-TR-2010-12.

[13] H. K. Khalil, *Nonlinear Systems*, 2nd ed. Upper Saddle River, NJ:: Prentice Hall, 1996.

[14] R. Lorenz, T. Lipo, and D. Novotny, "Motion control with induction motors," *Proc. IEEE*, vol. 82, no. 8, pp. 1215 –1240, Aug. 1994.

[15] W. Leonhard, *Control of Electrical Drives*, 3rd ed. Berlin: Springer-Verlag, 2001.

[16] O. Wasynczuk, S. Sudhoff, K. Corzine, J. Tichenor, P. Krause, I. Hansen, and L. Taylor, "A maximum torque per ampere control strategy for induction motor drives," *IEEE Trans. Energy Convers.*, vol. 13, no. 2, pp. 163 –169, June 1998.

[17] M.-H. Shin, D.-S. Hyun, and S.-B. Cho, "Maximum torque control of stator-flux-oriented induction machine drive in the field-weakening region," *IEEE Trans. Ind. Appl.*, vol. 38, no. 1, pp. 117 –122, 2002.

[18] I. Wallace, D. Novotny, R. Lorenz, and D. Divan, "Verification of enhanced dynamic torque per ampere capability in saturated induction machines," *IEEE Trans. Ind. Appl.*, vol. 30, no. 5, pp. 1193 –1201, 1994.

[19] C. Kwon and S. Sudhoff, "An improved maximum torque per amp control strategy for induction machine drives," in *Proc. IEEE Appl. Power Electron. Conf.*, vol. 2, 2005, pp. 740 –745.

[20] D. Casadei, F. Profumo, G. Serra, and A. Tani, "FOC and DTC: Two viable schemes for induction motors torque control," *IEEE Trans. Power Electron.*, vol. 17, no. 5, pp. 779 – 787, Sep. 2002.

[21] P. Krein, F. Disilvestro, I. Kanellakopoulos, and J. Locker, "Comparative analysis of scalar and vector control methods for induction motors," in *Proc. IEEE Power Electronics Specialists Conf.*, June 1993, pp. 1139 –1145.

[22] G. Kenne and, R. Simo, F. Lamnabhi-Lagarrigue, A. Arzand and, and J. Vannier, "An online simplified rotor resistance estimator for induction motors," *IEEE Trans. Control Systems Technology*, vol. 18, no. 5, pp. 1188 –1194, 2010.

[23] R. De Doncker and D. Novotny, "The universal field oriented controller," *IEEE Trans. Ind. Appl.*, vol. 30, no. 1, pp. 92 –100, 1994.

[24] X. Xu, R. De Doncker, and D. Novotny, "Stator flux orientation control of induction machines in the field weakening region," in *Conf. Rec. IEEE Ind. Appl. Soc. Annu. Meeting.*, Oct. 1988, pp. 437 –443.

[25] X. Xu, R. De Doncker, and D. Novotny, "A stator flux oriented induction machine drive," in *Proc. IEEE Power Electronics Specialists Conf.*, vol. 2, Apr. 1988, pp. 870 –876.

[26] A. Bazzi, A. Friedl, S. Choi, and P. Krein, "Comparison of induction motor drives for electric vehicle applications: Dynamic performance and parameter sensitivity analyses," in *Proc. IEEE Int. Electric Machines and Drives Conf. (IEMDC '09)*, May 2009, pp. 639 –646.

[27] R. Ortega, N. Barabanov, G. Escobar, and E. Valderrama, "Direct torque control of induction motors: Stability analysis and performance improvement," *IEEE Trans. Autom. Control*, vol. 46, no. 8, pp. 1209 –1222, Aug. 2001.

[28] C. Lascu, I. Boldea, and F. Blaabjerg, "Variable-structure direct torque control - A class of fast and robust controllers for induction machine drives," *IEEE Trans. Ind. Electronics*, vol. 51, no. 4, pp. 785 – 792, 2004.

[29] S.-K. Lin and C.-H. Fang, "Sliding-mode direct torque control of an induction motor," in *Proc. IEEE Ind. Electronics Soc. Conf. IECON '01.*, vol. 3, 2001, pp. 2171 –2177.

[30] D. Casadei, G. Serra, and A. Tani, "Improvement of direct torque control performance by using a discrete SVM technique," in *Proc. IEEE Power Electronics Specialists Conf.*, vol. 2, May 1998, pp. 997 –1003.

[31] T. Habetler, F. Profumo, M. Pastorelli, and L. Tolbert, "Direct torque control of induction machines using space vector modulation," *IEEE Trans. Ind. Appl.*, vol. 28, no. 5, pp. 1045 –1053, 1992.

[32] T. Habetler, F. Profumo, and M. Pastorelli, "Direct torque control of induction machines over a wide speed range," in *Conf. Rec. IEEE Ind. Appl. Soc. Annu. Meeting.*, Oct. 1992, pp. 600 –606.

[33] P. Grabowski and F. Blaabjerg, "Direct torque neuro-fuzzy control of induction motor drive. DSP implementation," in *Proc. IEEE Industrial Electronics Soc. Conf.*, vol. 2, Aug. 1998, pp. 657 –661.

[34] K. Hurst, T. Habetler, G. Griva, and F. Profumo, "Zero-speed tacholess IM torque control: Simply a matter of stator voltage integration," *IEEE Trans. Ind. Appl.*, vol. 34, no. 4, pp. 790 –795, 1998.

[35] M. Nillesen, J. Duarte, M. Pasquariello, and A. Del Pizzo, "Direct torque control with the application of a predictive pulse width control," in *Proc. IEEE Industry Applications Conf.*, vol. 3, 2000, pp. 1375 –1379.

[36] Y.-S. Lai and J.-C. Lin, "New hybrid fuzzy controller for direct torque control induction motor drives," *IEEE Trans. Power Electron.*, vol. 18, no. 5, pp. 1211 – 1219, 2003.

[37] Y. Xia and W. Oghanna, "Study on fuzzy control of induction machine with direct torque control approach," in *Proc. IEEE Int. Symp. on Industrial Electronics.*, vol. 2, July 1997, pp. 625 –630.

[38] J.-H. Lee, C.-G. Kim, and M.-J. Youn, "A dead-beat type digital controller for the direct torque control of an induction motor," *IEEE Trans. Power Electron.*, vol. 17, no. 5, pp. 739 – 746, Sep. 2002.

[39] K. Jezernik, "Hybrid DTC induction motor approach," in *Proc. IEEE Ind. Electronics Conf., IECON '09.*, 2009, pp. 2861 –2866.

[40] L. Zhou, "DSP-controlled direct torque control of induction machines based on modified integrator," in *Proc. IEEE Conf. Ind. Electronics and Appl, ICIEA*, May 2007, pp. 1790 –1793.

[41] Y. Wan, C. Hu, J. Zhao, S. Wan, and Y. Wang, "A new robust DTC-SVM for high performance induction machine drives," in *Proc. Int. Symp. Systems and Control in Aerospace and Astronautics ISSCAA*, 2008, pp. 1 –5.

[42] B.-S. Lee and R. Krishnan, "Adaptive stator resistance compensator for high performance direct torque controlled induction motor drives," in *Conf. Rec. IEEE IAS Annual Meeting*, vol. 1, Oct. 1998, pp. 423 –430.

[43] V. T. Buyukdegirmenci and P. T. Krein, "Direct torque control stability conditions and compensation methods," in *Proc. IEEE Int. Electric Machines and Drives Conf. (IEMDC '11)*, May 2011, pp. 643– 648.

[44] V. T. Buyukdegirmenci and P. T. Krein, "Control for high instantaneous torque from induction machines: Methods and Limits," in *Proc. IEEE Int. Electric Machines and Drives Conf. (IEMDC '11)*, May 2011, pp. 661– 666.

[45] G. Buja, D. Casadei, and G. Serra, "Direct stator flux and torque control of an induction motor: Theoretical analysis and experimental results," in *Industrial Electronics Society, 1998. IECON '98. Proceedings of the 24th Annual Conference of the IEEE*, vol. 1, Aug. 1998, pp. T50 –T64 vol.1.